Geophysical Journal International

Geophys. J. Int. (2014) **196,** 867–884
Advance Access publication 2013 November 20

doi: 10.1093/gji/ggt440

Seismoelectric coupling in unsaturated porous media: theory, petrophysics, and saturation front localization using an electroacoustic approach

A. Revil,[1,2] G. Barnier,[1] M. Karaoulis,[1] P. Sava,[1] A. Jardani[3] and B. Kulessa[4,*]

[1] *Department of Geophysics, Colorado School of Mines, Golden, CO* 80401, *USA. E-mail: arevil@mines.edu*
[2] *ISTerre, CNRS, UMR CNRS* 5275, *Université de Savoie,* 73376 *cedex, Le Bourget du Lac, France*
[3] *Université de Rouen, M2C, UMR* 6143, *CNRS, Morphodynamique Continentale et Côtière, Mont Saint Aignan, France*
[4] *College of Science, Swansea University, Swansea* SA2 0DJ, *United Kingdom*

Accepted 2013 October 22. Received 2013 October 21; in original form 2013 July 20

SUMMARY

The seismoelectric method is based on the interpretation of the electrical field associated with the conversion of mechanical to electromagnetic energy during the propagation of seismic waves in heterogeneous porous media. We propose an extension of a poroacoustic model that takes into account fluid flow and the effect of saturation. This model is coupled with an electrokinetic model accounting for the effect of saturation and in agreement with available experimental data in sands and carbonate rocks. We also developed new scaling laws for the permeability, the streaming potential coupling coefficient and the capillary entry pressure of porous media. The theory is developed for frequencies much below the critical frequency at which inertial effects starts to dominate in the Navier–Stokes equation (>10 kHz). The equations used to compute the propagation of the *P* waves and the seismoelectric effect in unsaturated condition are solved with finite elements using triangular meshing. We demonstrate the usefulness of a recently developed technique, seismoelectric beamforming, to localize saturation fronts by focusing seismic waves and looking at the resulting seismoelectric conversions. This method is applied to a cross-hole problem showing how a saturation front characterized by a drop in the electrical conductivity and compressibility is responsible for seismoelectric conversions. These conversions can be used, in turn, to determine the position of the front over time.

Key words: Electrical properties; Magnetic and electrical properties; Hydrogeophysics; Permeability and porosity; Wave propagation; Acoustic properties.

1 INTRODUCTION

The seismoelectric method has recently received a lot of attention because of its sensitivity to heterogeneities in mechanical, hydraulic and electrical properties (e.g. Hunt & Worthington 2000; Fourie 2003; Zhu *et al*. 2008; Jardani *et al*. 2010) and the detection of resonance effects in porous formations (see Revil & Jardani 2010 for heavy oils and Jougnot *et al.* 2013 for the presence of fractures). Since Pride (1994), most of the modelling efforts in computing the seismoelectric effect (e.g. Pride & Haartsen 1996; Haartsen & Pride 1997; Garambois & Dietrich 2002; Haines 2004; Hu *et al.* 2007) have been based on the following assumptions: (1) use of a Biot theory (Biot 1956a,b) in solving the equations for the solid and fluid displacements vectors, (2) solving the electromagnetic problem in the diffusive limit of the Maxwell equations and (3) using an electrokinetic theory based on the use of the zeta potential (a local electrostatic potential defined inside the electrical double layer coating the surface of the solid phase).

Revil, Jardani, and coworkers (Jardani *et al.* 2010; Revil & Jardani 2010; Araji *et al.* 2012; Revil & Mahardika 2013) have recently developed an alternative approach based on (1) solving the Biot theory in terms of the solid displacement vector and the fluid pressure (a classical approach in mechanics, e.g. Karpfinger *et al.* 2009, but curiously not used in the modelling of seismoelectric effects), (2) solving the electromagnetic problem in its quasi-static limit of the Maxwell equations and (3) used an electrokinetic theory based on the charge per unit pore volume as an alternative to the zeta-potential-based model. The advantages of this modelling approach are (1) the speed of the forward modelling is increased considerably because we are solving the hydromechanical equations for four unknowns in 3-D (six unknowns in the approach used by Pride and followers). (2) The speed of the electromagnetic forward problem is also drastically increased (solving a Poisson-type equation is indeed much faster than solving a diffusion-based problem and

*Formerly at: School of Civil Engineering, Queen's University Belfast, Belfast BT9 5AG, Northern Ireland.

© The Authors 2013. Published by Oxford University Press on behalf of The Royal Astronomical Society.

GJI Marine geosciences and applied geophysics
Downloaded from http://gji.oxfordjournals.org/ at Colorado School of Mines on July 1, 2015

reasonably accurate for the seismoelectric problem). (3) The model based on the volumetric charge density is using additional relationships between the charge density and the permeability, decreasing the total number of unknowns in the petrophysical model. This allows, as shown below, a straightforward extension of the theory at partial saturations. The gain taken in the computational speed of the forward problem has been used to implement different inversion algorithms based on complementary stochastic (Jardani *et al.* 2010) and deterministic (Araji *et al.* 2012) methods. Recently, Sava & Revil (2012) have proposed to use a poroacoustic approximation to speed up the computation of the seismoelectric problem for very complex geometries.

With the exception of Revil & Mahardika (2013) and Warden *et al.* (2013), all the seismoelectric theories (Pride 1994; Revil & Jardani 2010) have been developed in fully water-saturated conditions. The goal of this paper is to propose a simple yet accurate poroacoustic theory coupled with dynamic electrokinetic theory for partially saturated porous media. Unsaturated streaming potentials have also recently attracted some attention in looking at vadose zone transport properties (Mboh *et al.* 2012) and CO_2 sequestration (Vieira *et al.* 2012; Talebian *et al.* 2013).

We consider below a porous material (isotropic) with two immiscible pore fluids, air (or oil) and water, water being the wetting phase. The non-wetting phase is considered to be a good insulator. We neglect the electrical double layer associated with the air (oil)/water interface (Leroy *et al.* 2012) assuming that the surface area associated with this interface is much smaller than the charge density contribution associated with the minerals/water interface. The extension of the seismoelectric theory to unsaturated conditions is actually quite straightforward. It will be based on a combination of a simple, poroacoustic theory to which we added an extension of the electrokinetic theory in unsaturated conditions (Linde *et al.* 2007; Revil *et al.* 2007).

2 THEORY

2.1 Poroacoustic theory in saturated conditions

The propagation of a seismic wave in the acoustic approximation can be described in terms of a pressure perturbation $P(\mathbf{r}, t)$ (true pressure minus the equilibrium pressure) or in terms of a fluid displacement $\mathbf{u}(\mathbf{r}, t)$. The volume strain θ is related to the displacement by,

$$\theta = \frac{\Delta V}{V} = \nabla \cdot \mathbf{u}, \tag{1}$$

where $\Delta V / V$ represents a relative variation of volume of the porous material during the passage of the seismic wave. The compressibility of the material is defined, in isothermal conditions, as

$$\frac{1}{K_u} = -\frac{1}{V}\left(\frac{\partial V}{\partial P}\right)_{T, m_f}, \tag{2}$$

where P denotes the confining pressure (in Pa), m_f denotes the mass of fluid per unit volume of material and K_u denotes the bulk modulus (in Pa) of the porous material in undrained conditions. In this model, we will assume that we can compute the effect of the passage of a seismic wave on fluid flow in two steps: (1) An instantaneous deformation, in undrained conditions, during the passage of the seismic wave and (2) a slow deformation corresponding to the flow of the fluid in the pore space. The confining pressure (positive in compression) is related to the stress tensor $\mathbf{T}$ by,

$$P = -\frac{1}{3}\text{Trace } \mathbf{T}. \tag{3}$$

The modulus K_u (in Pa) is defined by (e.g. Wang 2000),

$$K_u = \frac{K_f (K_s - K) + \phi K \left(K_s - K_f\right)}{K_f(1 - \phi - K/K_s) + \phi K_s}, \tag{4}$$

where K_s and K_f denote the bulk moduli of the solid and fluid phases, respectively, K is the bulk modulus (in Pa) of the skeleton (drained bulk modulus) and ϕ denotes the connected porosity. The assumptions corresponding to these deformation of the porous material during the undrained deformation of the porous material are those of Gassmann theory (Gassmann 1951): (1) The porous material is macroscopically homogeneous, monomineralic and isotropic, (2) the pore space is interconnected and (3) the pore space is filled with a frictionless fluid (this is not the case during the flow of the pore fluid during the drained deformation of the material).
We use Hooke's law for the stress tensor,

$$\mathbf{T} = 3K_u \,\text{vol}(\varepsilon) + 2G \,\text{dev}(\varepsilon), \tag{5}$$

where $\text{vol}(\varepsilon)$ and $\text{dev}(\varepsilon)$ denote the volumetric strain tensor and the deviatoric (traceless) strain tensor, respectively, and G described the shear modulus of the skeleton (frame) of the porous material.. The macroscopic pressure perturbation is related to the displacement by,

$$P = -K_u \nabla \cdot \mathbf{u}. \tag{6}$$

However, to be compatible with the P-wave velocity, this equation needs to be replaced by,

$$P = -\left(K_u + \frac{4}{3}G\right)\nabla \cdot \mathbf{u}. \tag{7}$$

Such transformation is classical to adapt the elastic case to the acoustic approximation (e.g. Alkhalifah 1998, 2000, 2003). Eq. (5) corresponds to Hookes's law for in the acoustic approximation and is valid for small deformation ($\theta \ll 1$). To get the field equation for the pressure perturbation P, we need to combine this equation with Newton's law, which is given by,

$$-\nabla P + \mathbf{F} = \rho \,\ddot{\mathbf{u}}, \tag{8}$$

where $\mathbf{F}$ is a source force and $\rho = (1 + \phi)\rho_S + \phi\rho_f$ (in kg m^{-3}) denotes the bulk density of material, ρ_S and ρ_f denote the mass densities of the solid and pore solution, respectively, and $\ddot{\mathbf{u}}$ corresponds to the acceleration of the seismic wave. As we need to express the divergence of the displacement in terms of pressure, we want to take the divergence of eq. (8). This yields,

$$-\nabla \cdot \left(\frac{1}{\rho}\nabla P\right) + \nabla \cdot \left(\frac{1}{\rho}\mathbf{F}\right) = \frac{\partial^2}{\partial t^2}\left(\nabla \cdot \mathbf{u}\right), \tag{9}$$

$$-\nabla \cdot \left(\frac{1}{\rho}\nabla P\right) + \nabla \cdot \left(\frac{1}{\rho}\mathbf{F}\right) = -\frac{1}{K_u + \frac{4}{3}G}\left(\frac{\partial^2 P}{\partial t^2}\right), \tag{10}$$

$$\frac{\partial^2 P}{\partial t^2} - \left(K_u + \frac{4}{3}G\right)\nabla \cdot \left(\frac{1}{\rho}\nabla P\right) = -\left(K_u + \frac{4}{3}G\right)\nabla \cdot \left(\frac{1}{\rho}\mathbf{F}\right), \tag{11}$$

which yields the acoustic wave equation with inhomogeneous source term $f(\mathbf{r}, t)$, that specifies the location and time history of the source

$$\frac{\partial^2 P}{\partial t^2} - \left(K_u + \frac{4}{3}G\right)\nabla \cdot \left(\frac{1}{\rho}\nabla P\right) = f(\mathbf{r}, t), \tag{12}$$

Downloaded from http://gji.oxfordjournals.org/ at Colorado School of Mines on July 1, 2015

$$f(\mathbf{r}, t) = -\left(K_u + \frac{4}{3}G\right)\nabla \cdot \left(\frac{1}{\rho}\mathbf{F}\right). \tag{13}$$

If we wish to determine the displacement of the fluid, we can, for instance, consider a wave with a sinusoidal time dependence given by,

$$P(\mathbf{r}, t) = P_\omega(\mathbf{r})\exp(-\mathrm{i}\omega t), \tag{14}$$

where i denotes the pure imaginary number and ω is the angular frequency. Inserting eq. (14) into the acoustic equation, neglecting the spatial variation in the density and the source term, shows that the amplitudes of the seismic waves obey the scalar Helmholtz equation,

$$\nabla^2 P_\omega(\mathbf{r}) + \frac{\omega^2}{c_p^2} P_\omega(\mathbf{r}) = 0, \tag{15}$$

$$c_p = \left(\frac{K_u + \frac{4}{3}G}{\rho}\right)^{\frac{1}{2}}. \tag{16}$$

If we consider Newton's law, eq. (8), we obtain the following equation for the displacement of the fluid,

$$\mathbf{u}(\mathbf{r}, t) = -\frac{1}{\rho\omega^2}\nabla p_\omega(\mathbf{r})\exp(-\mathrm{i}\omega t). \tag{17}$$

Because the curl of a gradient is always equal to zero, we have the property $\nabla \times \mathbf{u}(\mathbf{r}, t) = 0$. The displacement is irrotational, which means that the pressure wave is purely longitudinal and corresponds to a P wave with a seismic velocity given by eq. (16).

The harmonic pressure is sketched in Fig. 1. It is responsible for areas of dilation and contraction of the porous material (Fig. 1a). In turn, these areas of dilation and contraction are going to be responsible for change in the fluid pressure as the fluid stay in contact with the solid during the deformation of the material. Now, we need to express the pressure change on the material to a pore fluid pressure change. In the undrained regime of poroelasticity, the pressure P is related to the so-called undrained pore fluid pressure p by (e.g. Wang 2000),

$$p = B\,P, \tag{18}$$

where $0 \leq B \leq 1$ is called the Skempton coefficient given by,

$$B = \frac{1 - K/K_u}{1 - K/K_S}, \tag{19}$$

where K_u is the undrained bulk modulus (in Pa), and K_S the bulk modulus of the solid phase (in Pa). The passage of the wave generates a confining pressure fluctuations P to a representative elementary volume of the rock. This change in confining pressure generates, in turn, a change in the pore fluid pressure and, therefore, the flow of the pore water (Figs 1b and c). Darcy's law provides the needed constitutive equation to determine the flux of water through the porous material,

$$\dot{\mathbf{w}} = -\frac{k_S}{\eta_f}\nabla p, \tag{20}$$

where $\mathbf{w}$ denotes the averaged fluid–solid relative displacement vector (in m), $\dot{\mathbf{w}}$ denotes the Darcy velocity (flux of water in a Lagrangian framework associated with the deformation of the skeleton), k_S denotes the permeability at saturation and η_f represents the dynamic viscosity of the pore fluid.

In summary, the properties entering the poroacoustic approximation used above are the undrained bulk modulus K_u, the drained modulus of the skeleton K, the bulk modulus of the pore fluid K_f,

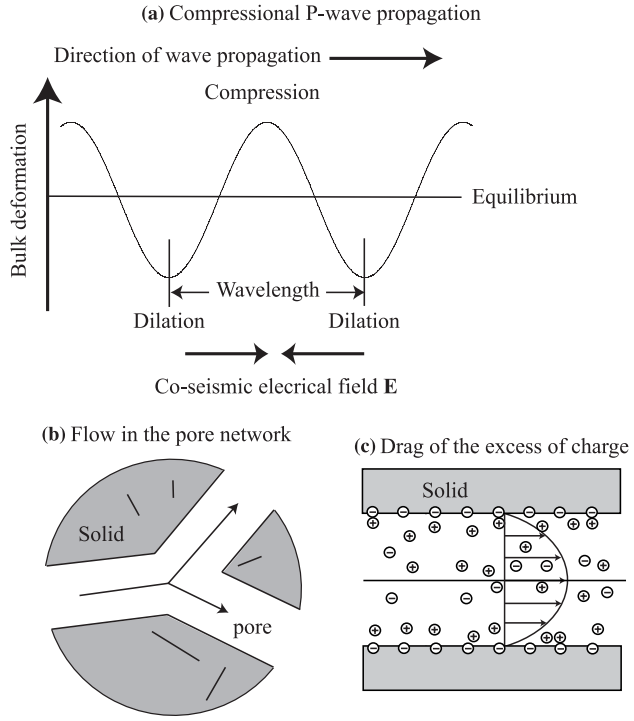


Figure 1. The coseismic electrical field and the coseismic (streaming) electrical current. (a) The propagation of a compressional (pressure or P) wave through a porous material generates areas of compression and dilation (expansion). (b) In response to the change in the mechanical stresses, the pore water flows from the compressed regions to the dilated regions. (c) The flow generates a streaming current density that is locally counterbalanced by the conduction current density creating, locally, an electrical field $\mathbf{E}$ of electrokinetic nature.

the shear modulus G (which is equal to the shear modulus of the skeleton), the permeability at saturation k_S and finally the dynamic viscosity of the pore fluid η_f. In unsaturated conditions, we will need to expand these properties as a function of saturation.

2.2 Dynamic electrokinetic theory at saturation

The flow of the pore water drags the excess of charge contains in the pore water generating a streaming current density (Figs 1b and c). The electrical field associated with the passage of a seismic wave through an electrical sensor is called the coseismic field. We consider the occurrence of the associated electrical disturbances in the quasi-static limit of the Maxwell equations as commonly done in self-potential studies. Using the electrokinetic coupling model developed by Revil & Linde (2006) and Revil *et al.* (2007), the electric potential φ (in V) is obtained by solving the following elliptic equations (see details in Jardani *et al.* 2010; Revil & Jardani 2010),

$$\nabla \cdot (\sigma \nabla \varphi) = \nabla \cdot \mathbf{j}_S, \tag{21}$$

where the electrical field is given by $\mathbf{E} = -\nabla\varphi$ in the quasi-static limit of the Maxwell equations, σ (in S m^{-1}) denotes the electrical conductivity of the porous medium. The dynamic streaming current density $\mathbf{j}_S$ (in A m^{-2}) is given by,

$$\mathbf{j}_S = \hat{Q}_V \dot{\mathbf{w}} = -\frac{\hat{Q}_V k_S}{\eta_f}\nabla p, \tag{22}$$

where $\dot{\mathbf{w}}$ denotes the Darcy velocity (volumetric flux of water) and $\hat{Q}_V$ denotes the effective charge per unit pore volume that is dragged

Downloaded from http://gji.oxfordjournals.org/ at Colora Mines on July 1, 2015

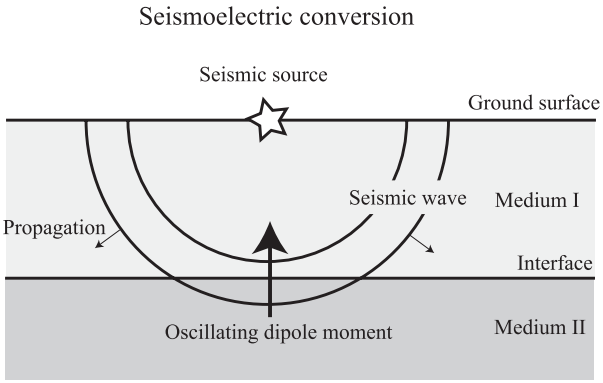


Figure 2. The seismoelectric conversion (called sometimes the interface response) results from the generation of an unbalanced source current density at an interface during the passage of a seismic wave. The divergence of the source current density at the interface is mathematically similar to an oscillating dipole moment generated at the interface in the first Fresnel zone. The star represents the position of the seismic source.

by the flow of the pore water relatively to the solid phase. This parameter is related to the permeability by $\log_{10} \hat{Q}_V = -9.2349 - 0.8219 \log_{10} k_0$ (see Jardani *et al.* 2010; Revil & Jardani 2010; Revil & Mahardika 2013). We neglect inertial terms, which is a pretty good approximation if we are dealing with frequencies below 5 kHz (see Revil & Mahardika 2013, for an example of calculation showing the importance of the inertial terms). The electrical potential φ (in V) is governed by the following Poisson equation:

$$\nabla \cdot (\sigma \nabla \varphi) = \Im, \tag{23}$$

$$\Im \equiv \nabla \cdot \mathbf{j}_S = -\nabla \cdot \left[\frac{\hat{Q}_V k_S}{\eta_f} \nabla (BP) \right]. \tag{24}$$

Solving eqs (23) and (24) is required to understand the electrical disturbance associated with the passage of a seismic wave through a heterogeneity, such as an interface (Fig. 2). In this case, the electrical field is called the seismoelectric conversion.

At saturation, the electrical conductivity of the porous material is given by (Revil 2013),

$$\sigma = \frac{1}{F}\sigma_w + \left(\frac{1}{F\phi}\right) \rho_S \beta_{(+)} (1 - f) \mathrm{CEC}, \tag{25}$$

where CEC denotes the Cation Exchange Capacity of the porous material, $\beta_{(+)}$ denotes the mobility for the counterions in the diffuse layer, F denotes the electrical formation factor and f ($0 \leq f \leq 1$) denotes the partition coefficient of the counterions in the Stern layer (fraction of counterions present in the Stern layer). The last term of eq. (25) corresponds to conduction in the electrical diffuse layer coating the surface of the grains and is called surface conductivity σ_S in the literature (see Waxman & Smits 1968).

In summary, the properties entering the electrical problem are the effective charge density $\hat{Q}_V$, the formation factor F and the surface conductivity corresponding to the last term of eq. (25). These three parameters will be explicitly related to the saturation in the next sections.

2.3 Influence of saturation

We consider an unsaturated material with two immiscible fluid phases: water that is considered the wetting phase for the solid and a non-wetting and insulating fluid phase like air or oil. The density of the pore fluid ρ_f depends on saturation according to $\rho_f = (1 - s_w)\rho_g + s_w \rho_w$, where s_w denotes the saturation of the water phase, ρ_g and ρ_w denote the mass density of the gas (or oil) and water phases, respectively. The undrained bulk modulus K_u, the bulk modulus of the pore fluid K_f and the dynamic viscosity of the pore fluid η_f are related to the properties of the gas (subscript g) and water (subscript w) by the following relationships (e.g. Rubino & Holliger 2012; Revil & Mahardika 2013):

$$K_u(s_w) = \frac{K_f(s_w)(K_s - K) + s_w \phi K \left(K_s - K_f(s_w)\right)}{K_f(s_w)(1 - \phi - K/K_s) + \phi K_s}, \tag{26}$$

$$K_f(s_w) = \left(\frac{1 - s_w}{K_g} + \frac{s_w}{K_w} \right)^{-1}, \tag{27}$$

$$\eta_f(s_w) = \eta_g \left(\frac{\eta_w}{\eta_g} \right)^{s_w}, \tag{28}$$

where eq. (27) corresponds to Wood's formula (Wood 1930) and eq. (28) can be found in Teja & Rice (1981). The Wood formula is not valid at low seismic frequencies. Indeed, it neglects mass conversion and heat transfer effects between fluid phases. Wood formula assumed that the two fluid phases are 'frozen'. For low gas saturations, the bulk modulus of the two fluids mixture predicted by the Wood model and the Landau–Lifshitz model (which accounts for transfer between the fluid phases, e.g. condensation) is expected to differ significantly. The saturation dependence of the Skempton coefficient depends on the saturation dependence of K_u.

We consider that the capillary pressure is at equilibrium (the deformation of the meniscus under the flow of the fluid phases is neglected). The saturation can be related to the capillary pressure by the Brook and Corey relationship,

$$s_w = \begin{cases} s_r + (1 - s_r) \left(\frac{p_e}{p_c}\right)^{\lambda}, & p_c \geq p_e \\ 1, & p_c < p_e \end{cases}, \tag{29}$$

or alternatively $p_c = p_e s_e^{-1/\lambda}$ (or $s_e = (p_c/p_e)^{-\lambda}$, $p_c \geq p_e$, see eq. (12) of Brooks & Corey 1964), where $s_e = (s_w - s_r)/(1 - s_r)$ denotes the effective or reduced water saturation, s_r the irreducible water saturation, p_c the capillary pressure and p_e the capillary entry pressure (critical pressure needed to displace the water phase by the gas phase when the porous material is fully water saturated). The entry pressure will be related to the permeability at saturation in Section 3.

We need to determine now the effect of the saturation on the electrical conductivity. We investigate here two models:

$$\sigma = \frac{1}{F} s_w^n \sigma_w + s_w^{n-1} \sigma_S \quad \text{(Model A)}, \tag{30}$$

$$\sigma = \frac{1}{F} s_w^n \sigma_w + \sigma_S \quad \text{(Model B)}, \tag{31}$$

where n is called the saturation exponent (Archie 1942) and σ_S denotes the surface conductivity at saturation. Model A is discussed in detail in Revil (2013) and was used for the seismoelectric problem by Revil & Mahardika (2013). It is also consistent with the Waxman & Smits (1968) model for unsaturated siliciclastic materials. The saturation dependence of Model B was proposed for the seismoelectric coupling in unsaturated conditions by Warden *et al.* (2013, see their eq. 13).

The effect of saturation on the excess of electrical charges per unit volume is taking by extending the empirical relationship between these two parameters in unsaturated conditions (see Linde *et al.* 2007; Revil *et al.* 2007):

$$\hat{Q}_V(s_w) = \frac{\hat{Q}_V}{s_w}. \tag{32}$$

Downloaded from http://gji.oxfordjournals.org/ at Colorado School of Mines on July 1, 2015

This equation has been recently challenged by Jougnot *et al.* (2012) but seems however to be consistent with experimental data as checked by Linde *et al.* (2007), Revil *et al.* (2007) and Mboh *et al.* (2012). We will show later that this model is also consistent with the data from Guichet *et al.* (2003), Revil *et al.* (2011) and Vinogradov & Jackson (2011).

3 ADDITIONAL SCALING RELATIONSHIPS

3.1 Relative permeability

In this section, we developed a unified set of scaling relationship between the hydraulic and electrical properties in order to reduce the number of input parameters. Three scaling laws are developed below, one for the relative water permeability, one for the capillary entry pressure and one for the streaming potential coupling coefficient. For each new scaling law, we will show that it is in agreement with existing experimental data or empirical scaling laws based on fitting experimental data.

The first type of scaling concerns the relationship between the electrical conductivity and the permeability. It is customary to define the following canonical boundary value problem for the normalized potential Γ for a cylindrical representative elementary volume of porous material of length L (see Pride 1994),

$$\nabla^2\Gamma = 0 \text{ in } V_p, \tag{33}$$

$$\hat{n}\cdot\nabla\Gamma = 0 \text{ on } S, \tag{34}$$

$$\Gamma = \begin{cases} L & \text{at } z = L \\ 0 & \text{at } z = 0 \end{cases} \text{ on } S, \tag{35}$$

and where z denotes the position along the cylindrical representative elementary volume in its axial direction. In these equations, $\hat{n}$ denotes the unit vector normal to the pore water/mineral interface S and V_p corresponds to the pore volume. The boundary conditions defining the normalized potential Γ are representative for the injection of an electrical current into a rock sample in the absence of surface conduction along the pore/water interface (see Johnson *et al.* 1986; Avellaneda & Torquato 1991; Pride 1994). The dynamic pore radius Λ and the formation factor F are defined as (Johnson *et al.* 1986):

$$\frac{2}{\Lambda} = \frac{\int_S |\nabla\Gamma|^2\,\mathrm{d}S}{\int_{V_p} |\nabla\Gamma|^2\,\mathrm{d}V_p}, \tag{36}$$

$$\frac{1}{F} = \frac{1}{V}\int_{V_p} |\nabla\Gamma|^2\,\mathrm{d}V_p, \tag{37}$$

where V is the total volume of the considered representative elementary volume. The length scale Λ corresponds, therefore, to a weighted version of the hydraulic pore radius V_p/S weighted by the norm of the electrical field (normalized by the electrical field imposed from the boundary of the material) and, therefore, Λ can be seen as the characteristic pore size of the porous body. From eq. (37), $1/F$ appears as dynamic porosity as discussed by Revil & Cathles (1999).

Using a volume-averaging approach, Johnson *et al.* (1986) and Pride (1994) developed the following equation for the electrical conductivity for a water-saturated rock:

$$\sigma = \frac{1}{F}\left(\sigma_w + \frac{2}{\Lambda}\Sigma_S\right), \tag{38}$$

where Λ is the characteristic pore length scale defined above. The extension of this equation to unsaturated conditions is discussed in the Appendix.

A comparison with eqs (30) and (31) with eq. (38) implies that following scaling laws for the dependence of the formation factor and length scale Λ with the relative water saturation,

$$F \Leftrightarrow Fs_w^{-n}, \tag{39}$$

$$\Lambda \Leftrightarrow \Lambda s_w \quad \text{(Model A)}, \tag{40}$$

$$\Lambda \Leftrightarrow \Lambda s_w^n \quad \text{(Model B)}, \tag{41}$$

where n denotes the second Archie's exponent also called the saturation exponent (Archie 1942). The left side of eqs (39)–(41) indicates the parameters used to compute the electrical conductivity in fully saturation conditions, and on the right side, we have the scaling of the same parameters with saturation for unsaturated materials.

The permeability k is related to the formation factor F and the dynamic pore radius Λ by (Johnson *et al.* 1986):

$$k_0(s_w) = \frac{\Lambda(s_w)^2}{8F(s_w)}. \tag{42}$$

Therefore, the permeability should scale with the water saturation as,

$$k_0(s_w) = \frac{\Lambda^2}{8F}s_w^{2+n} \quad \text{(Model A)}, \tag{43}$$

$$k_0(s_w) = \frac{\Lambda^2}{8F}s_w^{3n} \quad \text{(Model B)}. \tag{44}$$

Therefore, according to this scaling the permeability can be computed as the product of the permeability at saturation $k_S = \Lambda^2/8F$ and a relative permeability that depends only on the relative water saturation:

$$k_0(s_w) = k_S k_r(s_w), \tag{45}$$

with

$$k_r(s_w) = s_e^{n+2} \quad \text{(Model A)}, \tag{46}$$

$$k_r(s_w) = s_e^{3n} \quad \text{(Model B)}, \tag{47}$$

where we used the effective water saturation s_e rather than the water saturation to enforce the fact that the relative permeability is null at the irreducible water saturation. These equations can be compared to the equations proposed by Li & Horne (2005, their eqs 5 and 6) $k_r(s_w) = s_e s_w^n$. In the Brooks & Corey (1964) model, the relative permeability is also given by a power law relationship (see also Purcell 1949),

$$k_r(s_w) = \left(\frac{p_c}{p_e}\right)^{-2-3\lambda} = s_e^r, \tag{48}$$

$$r = \frac{2+3\lambda}{\lambda}, \tag{49}$$

where λ is called the pore size distribution index. Therefore, we identify the following equalities

$$\lambda = \frac{2}{n-1}, \qquad r = n+2 \quad \text{(Model A)}, \tag{50}$$

$$\lambda = \frac{2}{3(n-1)}, \qquad r = 3n \quad \text{(Model B)}. \tag{51}$$

This result is very important because it provides an explicit relationship between a hydraulic parameter and an electrical parameter.

Downloaded from http://gji.oxfordjournals.org/ at Colora Mines on July 1, 2015

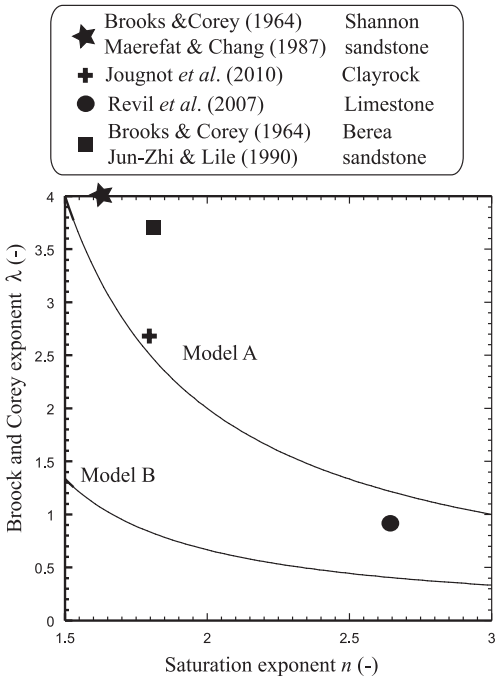


Figure 3. Comparison between Models A and B used to predict the value of the Books and Corey exponent l from the saturation exponent. Data from Jougnot *et al.* (2010), Revil *et al.* (2007), Brooks & Corey (1964), Maerefat & Chang (1987) (value extrapolated at ambient pressure and 25 °C) and Jun-Zhi & Lile (1990). The Shannon sandstone is also known under the term 'Hygiene sandstone' in the literature. For the Berea sandstone, the data of Maerefat & Chang (1987; their fig. 3) yield a very similar value than those of Jun-Zhi & Lile (1990) when extrapolated at 25 °C and ambient pressure. The data seem to favour Model A over Model B but more data are needed to test the models.

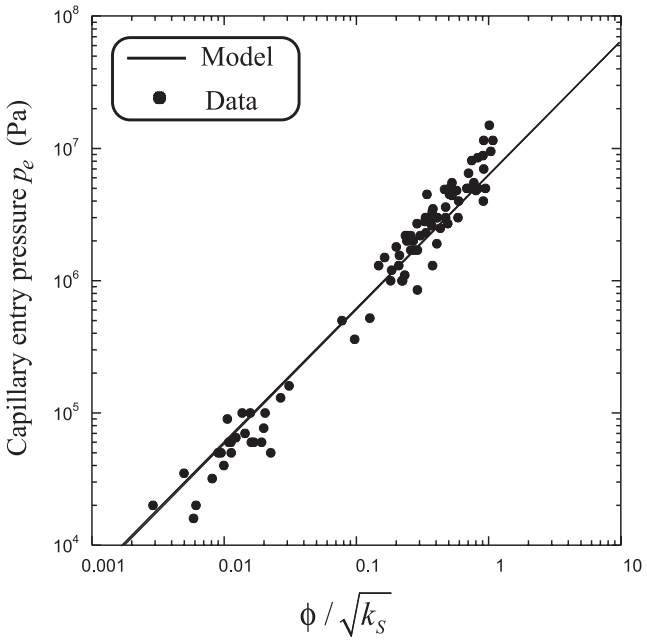


Figure 4. Comparison between the model proposed in the main text for the capillary entry pressure assuming that the formation factor is related to the porosity by $F = \phi^{-2}$ (classical Archie's law, Archie 1942). The experimental data are from Huet *et al.* (2005). They correspond to 89 sets of mercury-injection (Hg–air) capillary pressure data. Core samples include both carbonate and sandstone lithologies. The permeability is expressed in mD.

To our knowledge, this is the first time that these relationships are proposed despite some attempts to connect the resistivity index and the capillary pressure curves (see for instance Li & Horne 2005).

In Fig. 3, we have plotted a number of experimental data from the literature in terms of the Brooks and Corey exponent versus the saturation exponent. Note that both in the case of the data of Maerefat & Chang (1987) and those of Jun-Zhi & Lile (1990), we plotted the corresponding saturation exponent as functions of the Brooks and Corey parameter taken from Brooks & Corey (1964) for the Shannon and Berea sandstones both characterized by a narrow porosity range. Fig. 3 shows that Model A seems to agree better than Model B with experimental data but more data are needed to check the predictive capabilities of the two models. These new relationships also mean that the measurement of the second Archie's exponent can be used to predict the capillary pressure curve and hysteretic behaviour in the capillary pressure curve should imply a hysteretic behaviour in the value of n.

3.2 Capillary entry pressure

We now turn our attention to the capillary entry pressure. The capillary entry pressure is usually given by (Katz & Thompson 1987),

$$p_e = \frac{2\gamma}{r_c}, \tag{52}$$

where γ represents the surface tension between water and air $(71.99 \pm 0.05) \times 10^{-3}$ N m^{-1} and r_c represents the smallest pore of the set of largest pore percolating through the porous material (Katz & Thompson 1987). Katz & Thompson (1987) also developed a relationship between the permeability and the percolation length scale r_c using percolation principles: $k_S = r_c^2/(226F)$. A comparison with $k_S = \Lambda^2/8F$ yields $r_c \approx 5.3\ \Lambda$. Using the relationship between the length scale r_c and the permeability at saturation, $k_S = r_c^2/(226F)$, together with eq. (52), we obtain,

$$p_e = \frac{2\gamma}{\sqrt{226F}} k_S^{-0.5}. \tag{53}$$

This equation can be compared to the empirical equation derived by Thomas *et al.* (1968), $p_e = 52 k_S^{-0.43}$, with p_e expressed in kPa and k_S in mD. Archie's law $F = \phi^{-m}$ can be used to compute F from the porosity and the cementation exponent. Taking $m = 2.0$ (a default value for sandstones, see Revil *et al.* 1998, their fig. 5) and a porosity $\phi = 0.20$ (a reasonable average value), we obtain $p_e = a\, k_S^{-0.5}$ with $a = 61$ with p_e expressed in kPa and k_S in mD. We also obtain $p_e = b\phi/\sqrt{k_S}$. The proportionality between the capillary entry pressure and the ratio $\phi/\sqrt{k_S}$ is checked in Fig. 4. Therefore, eq. (53) is able to represent data but accounts explicitly for the porosity dependence, which is not the case of the empirical equation developed by Thomas *et al.* (1968).

3.3 Relative coupling coefficient with the Brooks and Corey model

The last coefficient we want to test is the streaming potential coupling coefficient, which can be defined for a fully water-saturated material as (Revil & Mahardika 2013),

$$C_0 = \lim_{\omega \to 0} \left(\frac{\partial \psi}{\partial p} \right)_{\mathrm{j}_S = 0} = \frac{\hat{Q}_V k_0}{\eta_w \sigma}. \tag{54}$$

Downloaded from http://gji.oxfordjournals.org/ at Colorado School of Mines on July 1, 2015

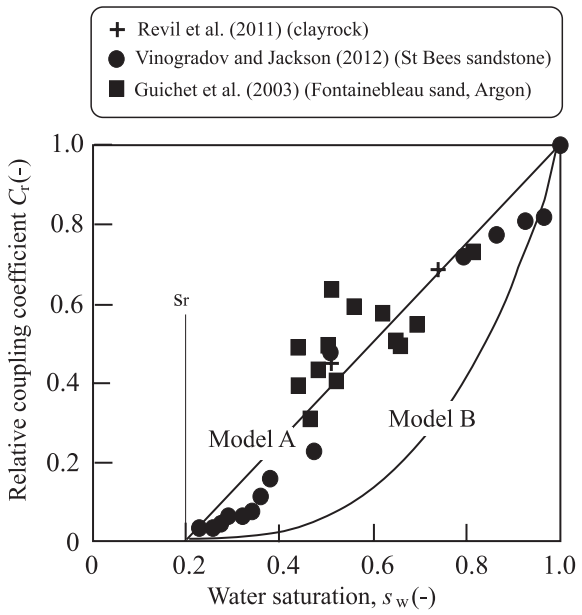


Figure 5. Comparison between Models A and B to predict the value of the relative streaming potential coupling coefficient as a function of the water saturation. We use an irreducible water saturation $s_r = 0.2$. Data from Revil *et al.* (2011), Vinogradov & Jackson (2011) and Guichet *et al.* (2003). The data seem to favour Model A over Model B.

At high salinity, the conductivity can be approximated by,

$$\sigma \approx \frac{1}{F} s_w^n \sigma_w. \tag{55}$$

We can now evaluate the effect of water saturation upon the streaming potential coupling coefficient by substituting inside eq. (54) the volumetric charge density, the permeability and the electrical conductivity by their expressions in function of the saturation. We obtain,

$$C_0 = C_r C_S, \tag{56}$$

where C_r denotes the relative coupling coefficient (a concept first introduced by Revil & Cerepi 2004) and where the streaming potential coupling coefficient at saturation is given by,

$$C_S = \frac{\hat{Q}_V k_0}{\eta_w \sigma}. \tag{57}$$

If eq. (57) is multiplied by $\rho_w g$ (g being the acceleration of the gravity in m s^{-2}), the coupling coefficient is expressed in V m^{-1}. The relative streaming potential coupling coefficient is given by,

$$C_r \approx s_e \qquad \text{(Model A)}, \tag{58}$$

$$C_r = s_e^{2n-1} \qquad \text{(Model B)}. \tag{59}$$

In Fig. 5, we compare the two models to the existing data replacing the water saturation by the irreducible saturation to satisfy to the additional constrain that there is no flow at the irreducible water saturation. Very clearly, Model B is unable to explain these data.

Note that the general form of the relative coupling coefficient with the Brooks and Corey model is,

$$C_r = s_w^{-(n+1)} s_e^{3+2/\lambda}, \tag{60}$$

as proposed by Revil *et al.* (2007, their eq. 112). In the next section, we will see how this equation needs to be modified if we use the Van Genuchten model, instead of the Brooks and Corey model, to represent the capillary pressure curve

Table 1. Petrophysical properties of the samples discussed in the main text. M corresponds to the sand sample investigated by Mboh *et al.* (2012) while samples E3 and E39 are dolomitic samples investigated by Revil *et al.* (2007).

Property	Symbol	M	E3	E39
Saturation exponent	n (–)	1.87	2.7	3.5
Cementation exponent	m (–)	–	1.93	2.49
Permeability	k (m^2)	8.4×10^{-12}	48.4×10^{-15}	23.8×10^{-15}
Porosity	ϕ (–)	0.41	0.203	0.159
Residual saturation	s_r (–)	0.09	0.31	0.34
Grain size	d (μm)	160	–	–
Pore size	r (μm)	–	1.18	0.17

3.4 Relative coupling coefficient with the Van Genuchten model

An alternative to the Brooks and Corey model is the Van Genuchten (1980) model (see discussion in Linde *et al.* 2007; Revil *et al.* 2007). This model can be written as,

$$s_e = \left(1 + \left|\frac{p_c}{p_e}\right|^{n_v}\right)^{-m_v} \quad \text{with } m_v \approx 1 - \frac{1}{n_v}, \quad p_c \geq p_e, \tag{61}$$

$$k_r(s_w) \approx \sqrt{s_e}\left[1 - (1 - s_e^{1/m_v})^{m_v}\right]^2, \tag{62}$$

where n_v and m_v are the Van Genuchten exponents. Therefore, the coupling coefficient is,

$$C_r = s_w^{-(n+1)} \sqrt{s_e}\left[1 - (1 - s_e^{1/m_v})^{m_v}\right]^2. \tag{63}$$

Mboh *et al.* (2012) measured the relative streaming potential coupling coefficient of a clean silica sand characterized by the following properties: 99.3 per cent silica, porosity $\phi = 0.41$, hydraulic conductivity $K = 8.25 \times 10^{-5}$ m s^{-1}, mean grain diameter $d = 160$ μm (Table 1). Their data are exceptionally good in terms of quality. It is indeed difficult to get very good data in unsaturated conditions because of the drift of the electrodes (see discussions in Revil & Linde 2011 and Jougnot & Linde 2013 for the drift associated with saturation effects and Petiau & Dupis 1980 and Petiau 2000, for other sources of noises). Their column was equipped with 10 non-polarizable Ag/AgCl electrodes and six T5 tensiometers and the acquisition were done at 1 kHz.

Mboh *et al.* (2012) measured a coupling coefficient at saturation of $C = -3.3$ mV m^{-1} for a pore water conductivity (tap water) of $\sigma_w = 0.044$ S m^{-1} at 25°C. The second Archie exponent (Saturation exponent) was measured and found to be equal to $n = 1.87$. The Van Genuchten exponent was measured and was found to be equal to $n_v = 3.88$ (by fitting the capillary pressure curve). This yields $m_v = 0.74$. A comparison between the data of Mboh *et al.* (2012) and eq. (62) is shown in Fig. 6. The best fit of the data yields $m_v = 0.69 \pm 0.05$; therefore, very close to the value determined from the capillary pressure curve (Fig. 6). As mentioned by Mboh *et al.* (2012), this implies that the values of the relative coupling coefficient bears information regarding the Van Genuchten parameters as suggested by Linde *et al.* (2007) and Revil *et al.* (2007).

In Figs 7 and 8, we reanalysed the data presented in Revil & Cerepi (2004) and Revil *et al.* (2007) correcting few mistakes in the unit conversions found in these two papers. We analysed the streaming potential coupling coefficient data of samples E3 and E39 (dolomitic limestones, see properties in Table 1). In both cases, the second Archie exponent (saturation exponent) was independently determined using resistivity measurements. The Van Genuchten parameters were found to be roughly the same using the capillary pressure curves and the relative streaming potential coupling coefficient data.

Downloaded from http://gji.oxfordjournals.org/ at Colora Mines on July 1, 2015

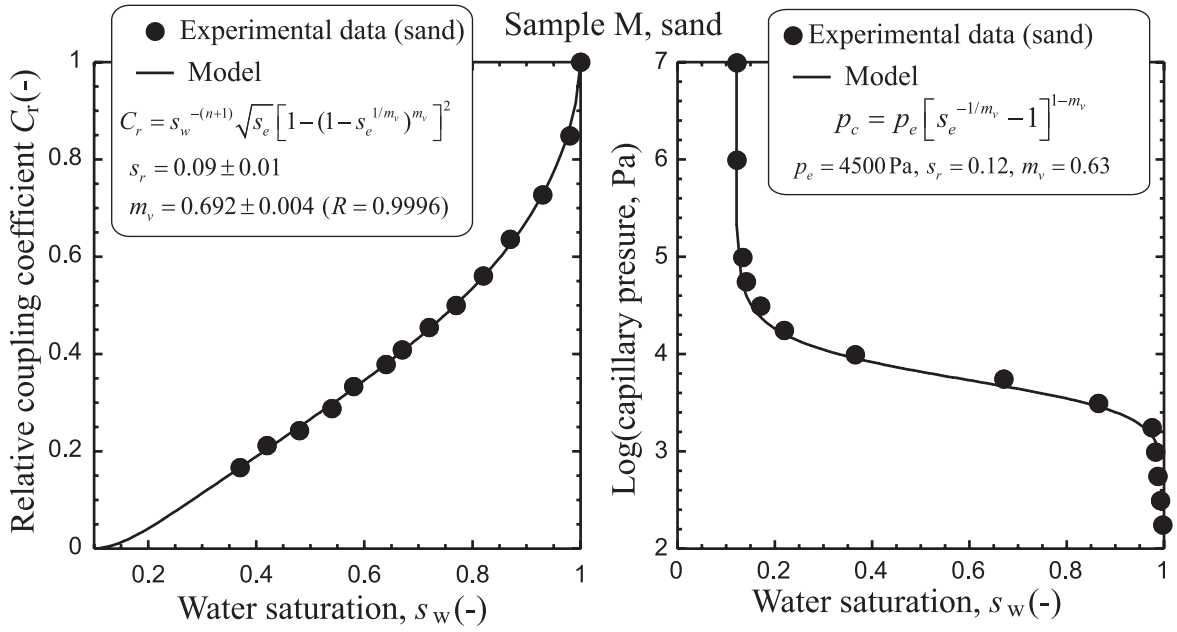


Figure 6. Comparison between experimental data and the prediction of the model developed by Revil *et al*. (2007) with the Van Genuchten model (see also Linde *et al.* 2007). The experimental data are from Mboh *et al.* (2012) (sample M, sand). Left panel: Relative streaming potential coupling coefficient versus saturation. We used the measured value of the saturation exponent (second Archie exponent) $n = 1.87$. Right panel: Capillary pressure curve (non-wetting fluid: air).

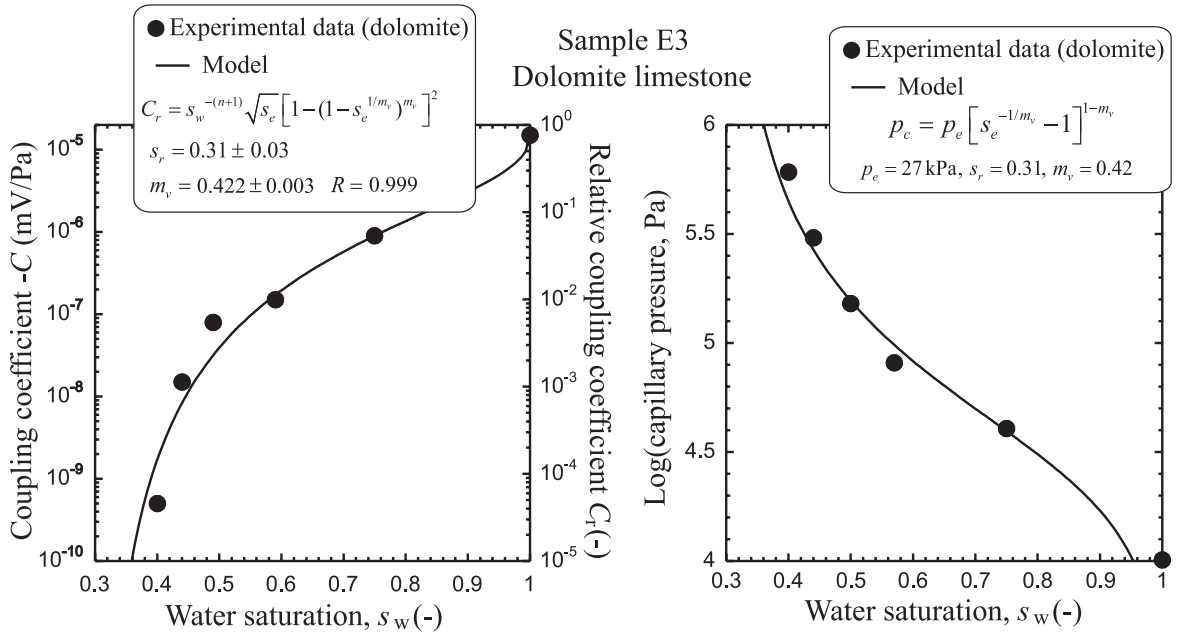


Figure 7. Comparison between experimental data and the prediction of the model developed by Revil *et al*. (2007) with the Van Genuchten model (see also Linde *et al.* 2007). The experimental data are from Revil & Cerepi (2004) and Revil *et al.* (2007) (sample E3). Left panel: Absolute and relative streaming potential coupling coefficient versus saturation. We used the measured value of the saturation exponent (second Archie exponent) $n = 2.7$. Right panel: Fit of the capillary pressure curve with the same Van Genuchten parameters than obtained for the coupling coefficient (non-wetting fluid: mercury).

4 SEISMOELECTRIC BEAMFORMING IN THE POROACOUSTIC APPROXIMATION

4.1 Motivation

We apply here the seismoelectric beamforming approach developed recently by Sava & Revil (2012) to localize a discontinuity in resistivity associated with a water saturation front. We consider a 2-D case where we modelled a background porous material with constant mechanical, hydraulic and electrical properties. Two rectangular heterogeneities (Anomalies 1 and 2) are embedded in this background as shown in Fig. 9. The background and the two anomalies share the same mechanical properties and only their hydraulic and electrical properties differ from one to another because of a change in saturation (the material properties are reported in Table 2). The background is supposed to be fully water saturated

Downloaded from http://gji.oxfordjournals.org/ at Colorado School of Mines on July 1, 2015

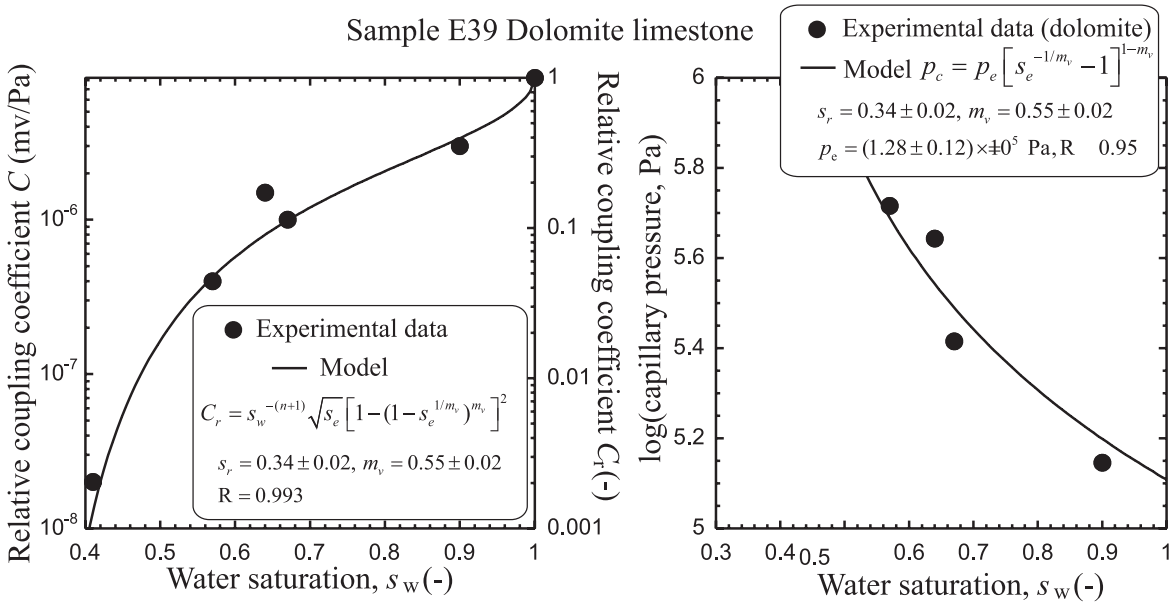


Figure 8. Comparison between experimental data and the prediction of the model developed by Revil *et al.* (2007) with the Van Genuchten model (see also Linde *et al.* 2007). The experimental data are from Revil & Cerepi (2004) and Revil *et al.* (2007) (sample E39). Left panel: Absolute and relative streaming potential coupling coefficient versus saturation. We used the measured value of the saturation exponent (second Archie exponent) $n = 3.5$. Right panel: Fit of the capillary pressure curve with the same Van Genuchten parameters than obtained for the coupling coefficient (non-wetting fluid: mercury).

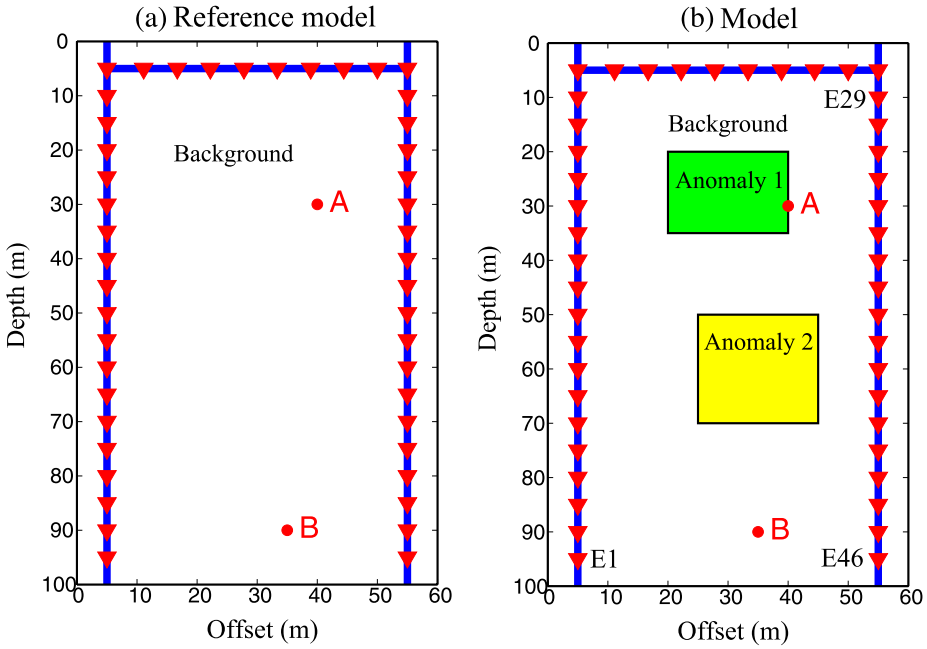


Figure 9. Geometry used for the beamforming problem. The medium consists of a homogeneous background model (reference model, fully saturated) plus two anomalies termed Anomaly 1 and Anomaly 2. These anomalies correspond to areas that are unsaturated (see Table 2). The survey area is surrounded by two vertical wells located on each side. The red triangles correspond to the location of the seismic sources/geophones/electrodes. The spacing between two consecutive sensors is 5 m. The two boreholes have 19 seismic set of sensors each and 8 additional set of sensors are located close to the ground surface (5 m deep). The two red-filled circles correspond to the focusing points used for our numerical experiments. E_i corresponds to the position of electrode i. They are 46 set of sensors in total with E1 and E46 are at the bottom of the two wells.

(electrical conductivity of 1 S m^{-1}) while the anomalies are more resistive (10^{-2} S m^{-1} for Anomaly 1 and 10^{-3} S m^{-1} for Anomaly 2 corresponding to two distinct saturations).

Seismic sources are located in two boreholes. The seismic sources (virtual geophones, seismic sources and electrodes) are set-up every 5 m along the ground surface and in the two wells (see Fig. 9, 19 sources in each well and 8 sources along the ground surface). Our objective is to beamform seismic waves at two specific points (positions A and B, see Fig. 9) and see if a seismoelectric conversion can be recorded by electrodes located in the wells in presence of a saturation front. When the seismic energy focuses on a heterogeneity, such as an interface, we expect to record a seismoelectric conversion (interface response). If we scan various points, this technique enables us to identify whether the point of focus is located close to a saturation front or not. The numerical experiment described below uses the acoustic approximation discussed in

Downloaded from http://gji.oxfordjournals.org/ at Colora Mines on July 1, 2015

Table 2. Petrophysical properties for the background and Anomalies 1 and 2.

Property	Background	Anomaly 1	Anomaly 2
Undrained bulk modulus K_u (Pa)	22×10^9	22×10^9	22×10^9
P-wave velocity V_p (m s^{-1})	3093	3093	3093
Excess charge density $\hat{Q}_V$ (C m^{-3})	0.20	2.0	6.7
Log (permeability, k in m^2)	–12	–14	–16
Skempton coefficient B	0.65	0.65	0.65
Average density ρ (kg m^{-3})	2300	2300	2300
Hydraulic viscosity of pore fluid β_f (Pa s)	10^{-3}	10^{-3}	10^{-3}
Conductivity σ (S m^{-1})	1	0.01	0.001
Saturation s_w (–)	1	0.10	0.03

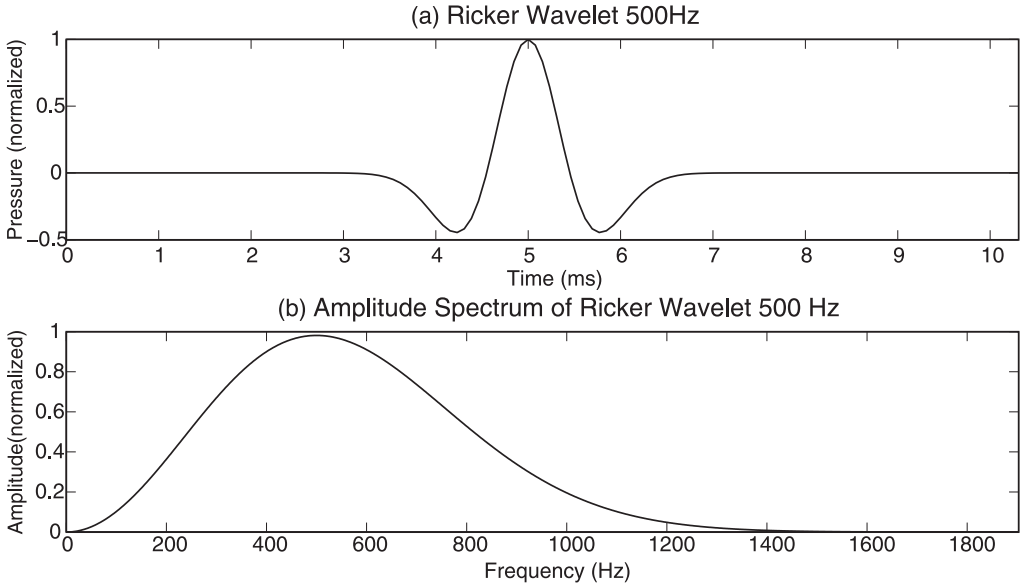


Figure 10. Pressure source $f(\mathbf{r}, t)$ (see eqs 12 and 13) used for the beamforming experiment. The pressure source is a Ricker wavelet with a 500 Hz dominant frequency and a time-shift of 5 ms. (a) Pressure time-series of the source. (b) Amplitude spectrum of the source.

Section 2 above. We solved the partial differential equations for the mechanical and electrical problems in the frequency domain.

4.2 Beamforming technique

The beamforming technique enables us to focus seismic energy at a desired location and at a known time knowing approximately the velocity model. As discussed in Sava & Revil (2012), the velocity model does not need to be perfectly known. The seismic beamforming is done in two steps:

Step 1: On a finite-element grid, we choose the point of focus and we insert a fictitious seismic point source at this location. The seismic source is a Ricker wavelet with a dominant frequency of 500 Hz (Fig. 10). It contains energy up to about 1500 Hz. Using a constant seismic P-wave velocity of 3100 m s^{-1}, we obtain a dominant wavelength of 6.2 m and a minimum wavelength of 2 m. That gives us a seismic resolution of 1.55 and 0.51 m, respectively. All numerical modellings were performed using the finite element package Comsol Multiphysics 4.3b using triangular meshing of non-constant element size (minimum element size of 0.0024 m and maximum element size of 1.2 m). This choice was driven by the need to have five elements of mesh per wavelength. In order to model the study areas without any seismic reflection at the boundaries (infinite medium), we used the CPML (convoluted perfect matched layer) developed by Jardani *et al.* (2010). The thickness of the CPML is 10 m around the area of interest. The seismic P waves are propagated from the source to fictitious electrodes located in place of the true seismic sources in the wells and along the ground surface. For one shot, we record the macroscopic pressure field $P_i(t)$ at each geophone i located in the wells.

Step 2: Once the pressure fields have been recorded at each geophone, we back propagate the pressure fields as shown in Fig. 11. We first flip the signal recorded at each geophone ($P_{\text{shifted}}(t) = P_{\text{recorded}}(T - t)$, where T is the total recording time or listening time). We then create seismic point sources located at the position of the virtual geophones and we reinject the flipped seismic signals into the medium. Those flipped outgoing pressure fields will then propagate and interfere constructively at the original location (where we first put the seismic source, see Fig. 11). During this back propagation, we record the electrical potential at the wells and along the ground surface at the 46 electrodes colocated with the seismic source.

The strength of this technique comes from the fact that we know exactly at what time and what location the seismic wavefields will focus and interfere constructively. If the point of focus is located on an interface, we will record an interface response with a greater amplitude that we would have recorded if there was only one wavefield crossing the interface. In fact, the electric potential diffused by a seismoelectric conversion due to a discontinuity in the medium properties is usually orders of magnitude smaller than the coseismic field (electrical field giving rise to an electrical13 potential only detectable inside the support of a seismic wave). An example is shown in Fig. 11(f) showing the dipolar field created by the beamforming of

Downloaded from http://gji.oxfordjournals.org/ at Colorado School of Mines on July 1, 2015

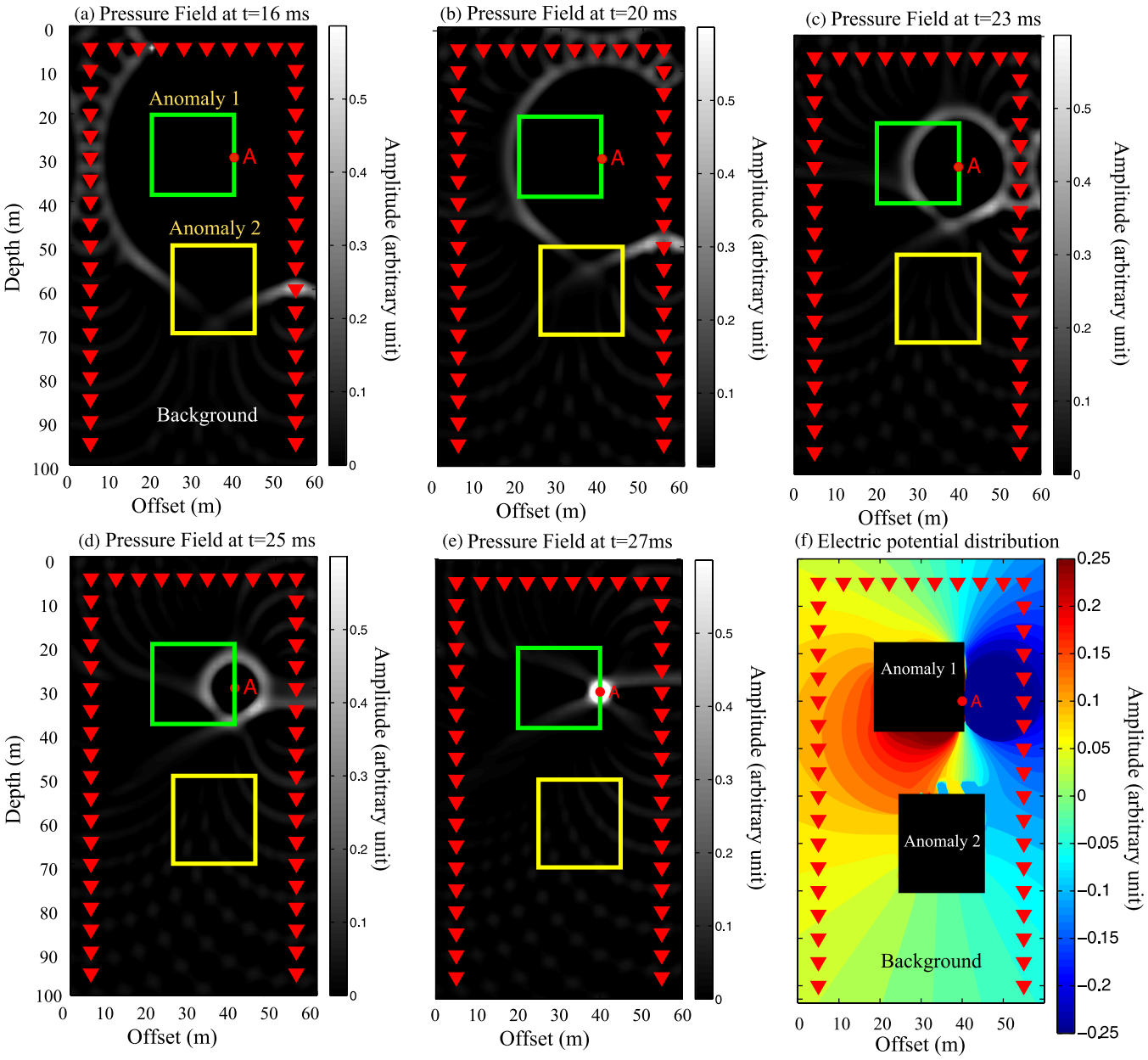


Figure 11. Seismic beamforming and resulting electrical potential distribution. (a)–(e). Snapshots showing the pressure field (coming from the 46 seismic sources shown in Fig. 9) focusing at point A. At $t = 27$ ms, the wavefield interfere constructively in point A and a strong seismoelectric is recorded at the receiver electrodes. (f) The distribution of the electrical potential (arbitrary units) corresponds to the case where the seismic energy is focused at point A. The seismoelectric conversion at the time of focusing is characterized by a strong dipolar behaviour.

the seismic waves at point A. This technique forces the interface response conversion to increase in amplitude due to the focusing of the different pressure fields coming from the multiple seismic sources.

By applying this technique to a grid of points within the survey area (by scanning the area point by point), we can then use the electrical response to map the discontinuities in terms of electrical and hydraulic properties of the material. We can also adjust and increase the resolution of our mapping by scanning over a denser grid of points around certain areas.

4.3 Results and interpretations

We focus seismic energy on few points of interests and we record the potential with 46 electrodes (19 in each borehole and 8 along the ground surface). The first point of focus (point A, see Figs 9 and 11) is located at an interface with a sharp discontinuity in conductivity and permeability. Therefore, we expect to see a seismoelectric conversion. Our results confirmed this assumption (Fig. 12). However, we need to remove the distribution of potential recorded with only the background to see the seismoelectric conversion associated with the interface response. We can clearly see that the dominant spike in the electric potential time-series (background removed) is perfectly synchronized with the focusing time of the seismic wavefield at point A. This enables us to detect a heterogeneity at point A.

Fig. 13 shows the electric potential at an electrode located at electrode E45 when the seismic wave are focused at point B, which is not located close to an interface. As expected, we see no spike at

Downloaded from http://gji.oxfordjournals.org/ at Colora Mines on July 1, 2015

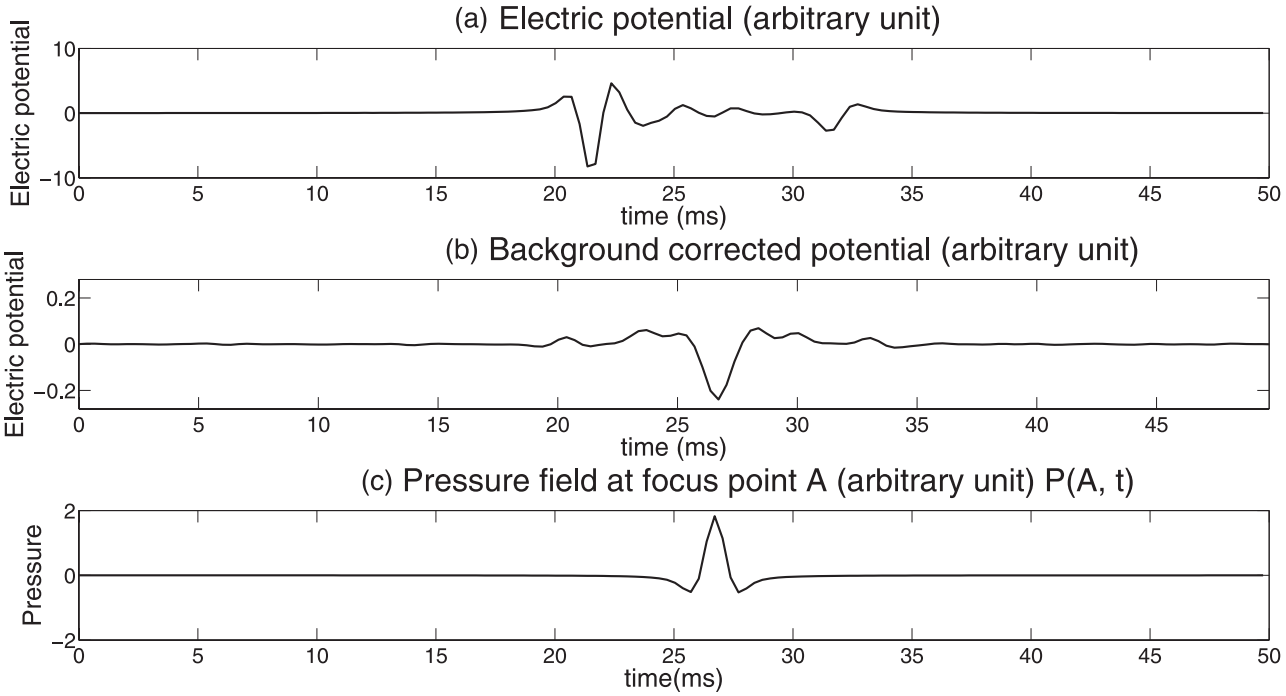


Figure 12. Beamforming at point A. (a) Time-series of the electrical potential at electrode E35 for beamforming the seismic wave at point A. The time-series comprise both the seismoelectric conversions and the coseismic field. The interface response is not detectable. (b) Electrical potential recorded when the medium contains the two anomalies minus the potential recorded if we only had the background. The interface response is now clearly visible. (c) Time-series of the pressure field at point B, $P(\mathrm{A}, t)$.

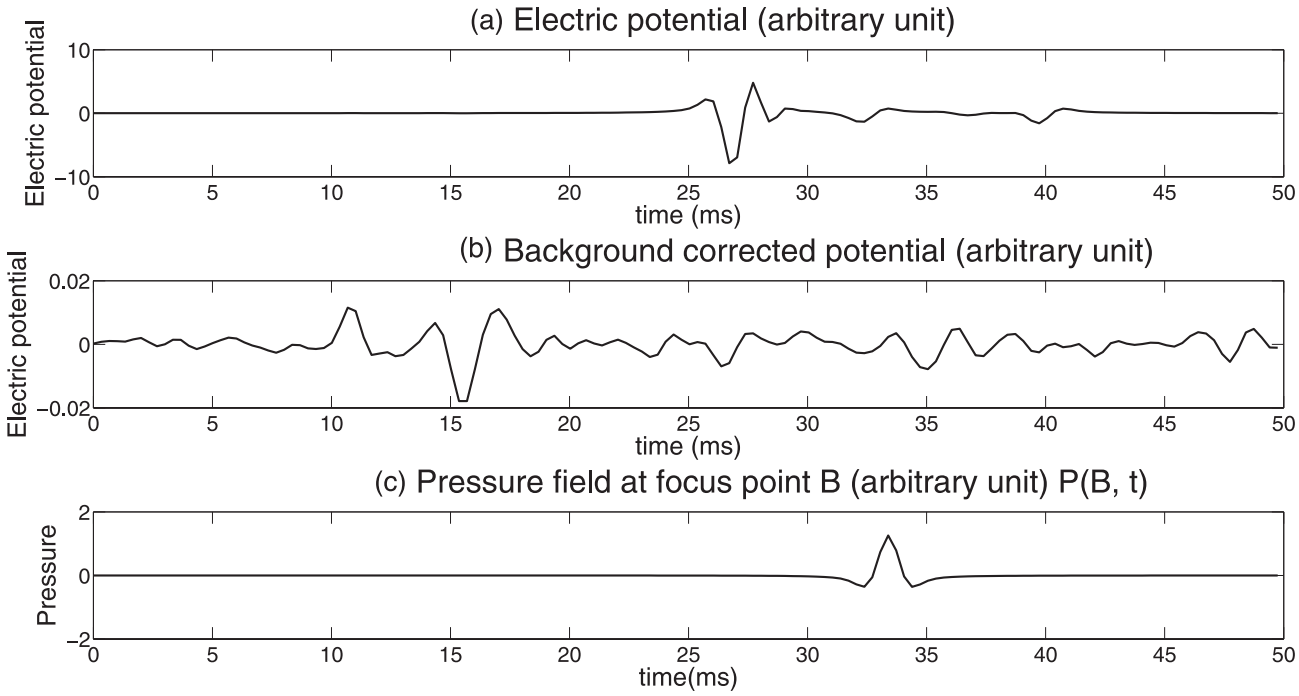


Figure 13. Beamforming at point B. (a) Time-series of the electrical potential at electrode E45. The time-series show both the seismoelectric conversions and the coseismic field. The interface response is not detectable. (b) Difference of two time-series: the electric potential in the top graph minus the electric potential recorded at the same location but for a homogeneous background (reference model). There is no conversion, which is consistent with the fact that point B is not associated with a heterogeneity. (c) Time-series of the pressure field at point B, $P(\mathrm{B}, t)$.

Downloaded from http://gji.oxfordjournals.org/ at Colorado School of Mines on July 1, 2015

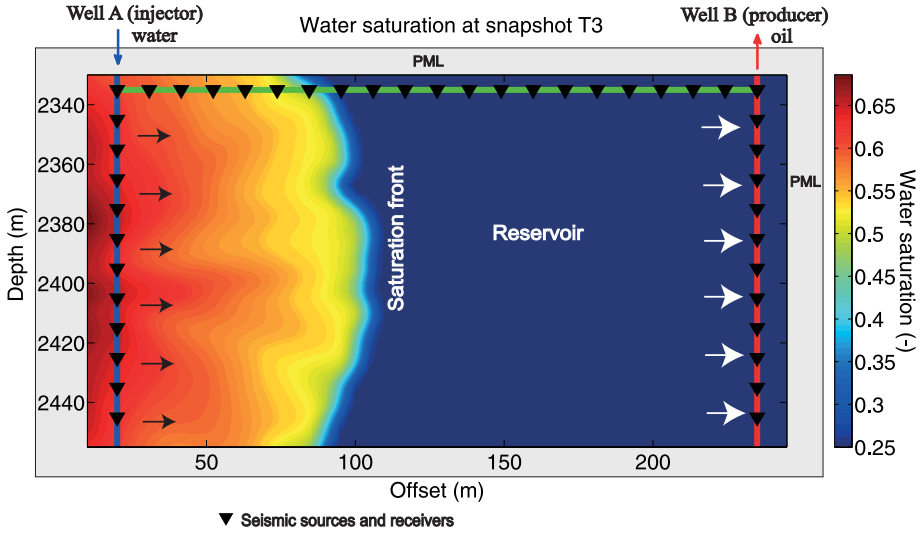


Figure 14. Sketch of the domain used for the modelling. The total modelling domain is a 410 m × 250 m rectangle. Injector Well A is used, located at position $x = 0$ m, is also used for the seismic source. Production and recording Well B is located at $x = 250$ m. The discretization of the domain comprises a finite element mesh of 205 × 125 rectangular cells. A total of 28 receivers are located in Well B, approximately 30 m away from the nearest PML boundary (the PML boundary layers are shown in grey).

the focus time, which indicates a lack of heterogeneity at the focus point. Therefore, this method can be used in time lapse to follow the evolution of a saturation front over time, for example, for CO_2 sequestration or to monitor water flooding experiments.

5 APPLICATION TO WATER FLOODING

In this section, we apply the approach taken in Section 4 to a more realistic scenario. A lot of work has been done recently in using low-frequency electrical signals to detect oil–water encroachment fronts (see, for instance, Saunders *et al.* 2008). We want to see if seismoelectric beamforming can be used to localize in a very simple way the position of the front. We consider two wells crossing a heterogeneous reservoir (see Fig. 14). Well B is located 250 m away from Well A and the total geometry of the model covers an area of 410 × 250 m. The reference position, O(0,0), is located at the upper-left corner of this domain. The reservoir is initially saturated with oil (oil saturation of 80 per cent). During water flooding operations, water is injected in Well A and oil is produced in Well B.

We use a random simulator to create a stochastic realization for the clay content and we use the model of Revil & Cathles (1999) to determine the porosity and the permeability at saturation. The multiphase flow simulator allows computing the saturation profiles, which are used to compute the *P*-wave velocity and resistivity distributions. The *P*-wave velocity and the permeability of the water phase are shown in Fig. 15 for snapshot 3, while the electrical conductivity and the porosity are shown in Fig. 16. The *P*-wave velocity does not depend too much on the saturation and its distribution is comprised between 4050 and 4300 m s^{-1}. The electrical conductivity distribution varies over an order of magnitude. The influence of the water saturation is much greater on the resistivity than on the *P*-wave velocity.

The seismic source is a Ricker wavelet (magnitude 1.0×10^4 N m, delay time $t_s = 30$ ms, dominant frequency $f_c = 160$ Hz). We solve the poroacoustic equations described in Section 2 and the Poisson equation for the electrical potential in the frequency domain. The material properties are described in Table 3. In summary,

Table 3. Material properties used in the saturation front detection. We use Model A with $m = n = 2$.

Parameter	Value	Units
ρ_s	2650	kg m^{-3}
ρ_w	1000	kg m^{-3}
ρ_o	900	kg m^{-3}
K_s	36.5	GPa
K	18.2	GPa
G	13.8	GPa
K_w	2.25	GPa
K_o	1.50	GPa
η_w	1×10^{-3}	Pa s
η_o	50×10^{-3}	Pa s

we compute the properties distributions given the porosity, fluid permeability and saturation distributions, then we solve for the confining pressure $P(\mathbf{r}, t)$ of the solid phase and the pore fluid pressure $p(\mathbf{r}, t)$. Finally, we compute the electrical potential by solving the Poisson equation coupled to the poroacoustic problem for the frequency range 8–800 Hz. This range is valid for our problem since the seismic wave and the associated electrical field operates in the same frequency range. We then compute the inverse Fourier transform (FFT^{-1}) to get the time-series of the seismic displacements u_x and u_z, and the time-series of the electric potential response.

The mesh is made of cell 2 × 2 m. The size of the mesh is smaller than the smallest wavelength of the seismic wave. For this mesh size, we check that the solution of the partial differential equations governing the seismoelectric problem is mesh independent. At the four external boundaries of the domain, we apply a 50-m-thick CPML.

Fig. 17 shows a pure transmission experiment between a seismic source located in Well A and an electrical receiver located in Well B. We also record the fluid pressure at the first Fresnel zone of the seismic wave at the position of the saturation front. Fig. 17 shows the existence of a strong seismoelectric conversion at the saturation front. This confirms the results of Revil & Mahardika (2013), who used a poroelastic theory.

Downloaded from http://gji.oxfordjournals.org/ at Colora Mines on July 1, 2015

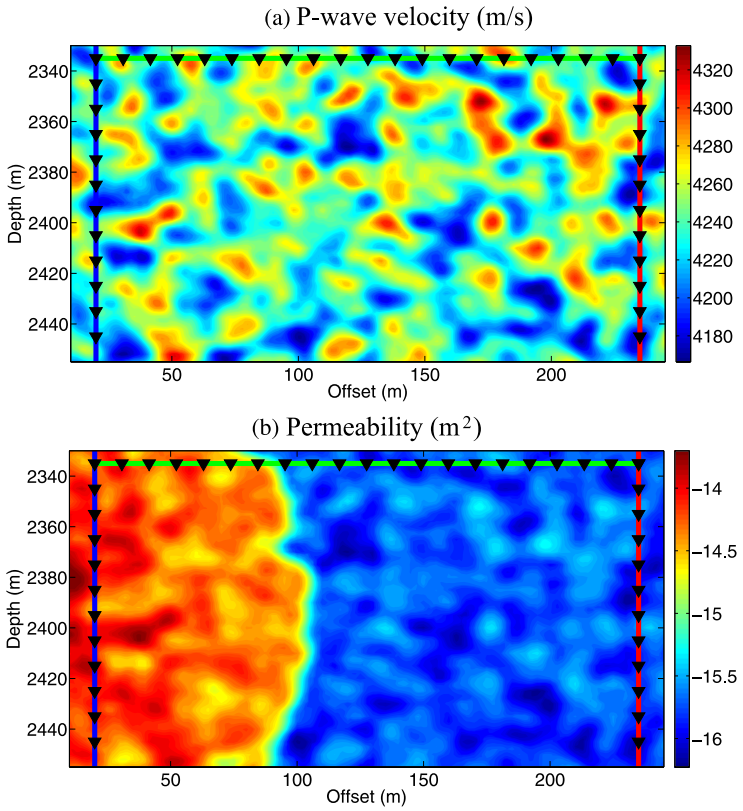


Figure 15. Sketch of the distribution of the *P*-wave velocity and permeability of the pore water phase at snapshop 3. Note that the saturation front is characterized by a sharp contract in permeability.

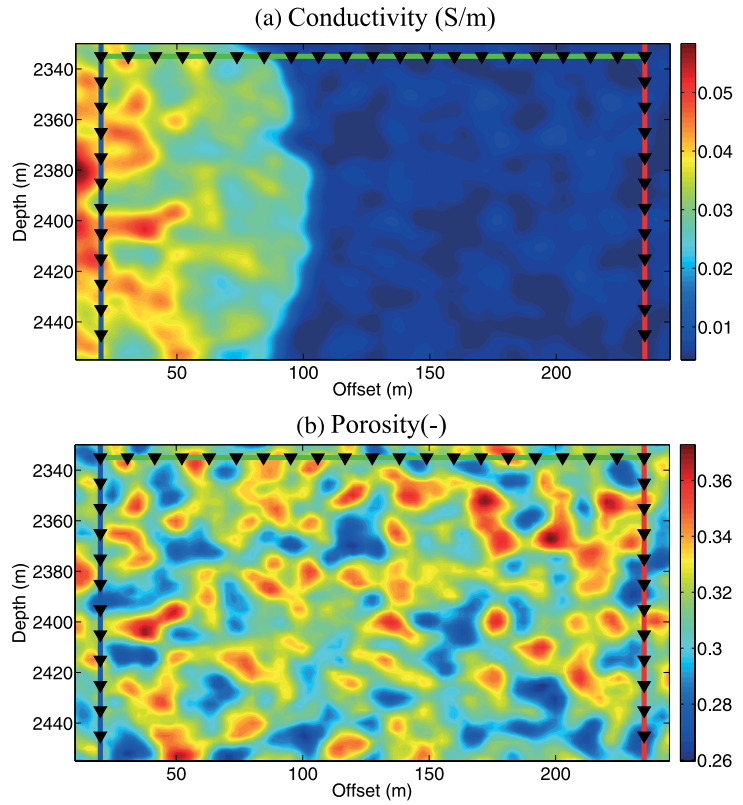


Figure 16. Sketch of the distribution of the electrical conductivity and porosity at snapshop 3. Note that the saturation front is characterized by a sharp contract in electrical conductivity.

Downloaded from http://gji.oxfordjournals.org/ at Colorado School of Mines on July 1, 2015

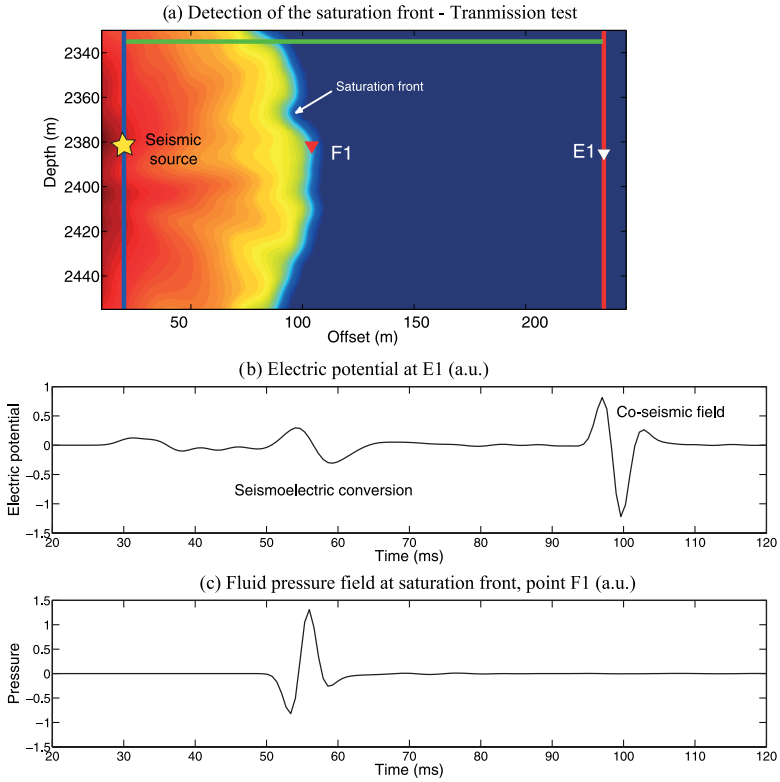


Figure 17. Transmission experiment with the seismic source in Well A and the electrical receiver in Well B. (a) Geometry of the test. (b) Time-series for the electrical potential showing the seismoelectric conversion occurring at the interface (like in Fig. 2) and the coseismic field (like in Fig. 1). (c) Fluid pressure field at a point located at the saturation front at the centre of the Fresnel zone.

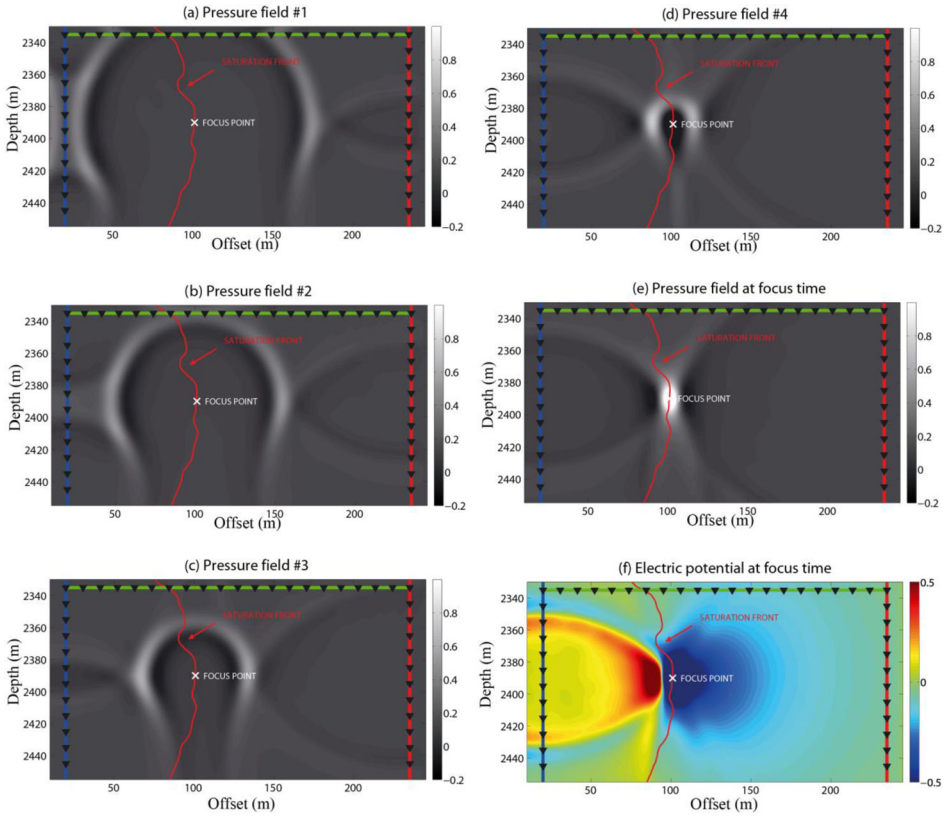


Figure 18. Seismic beamforming at the saturation front and resulting electrical potential distribution. (a)–(e) Evolution of the confining pressure $P(\mathbf{r},t)$ for five snapshots. The propagating wavefields interfere constructively at the focus point. (f) Electrical potential distribution corresponding to the seismic energy focused at the saturation front (snapshot e).

Downloaded from http://gji.oxfordjournals.org/ at Colorado School of Mines on July 1, 2015

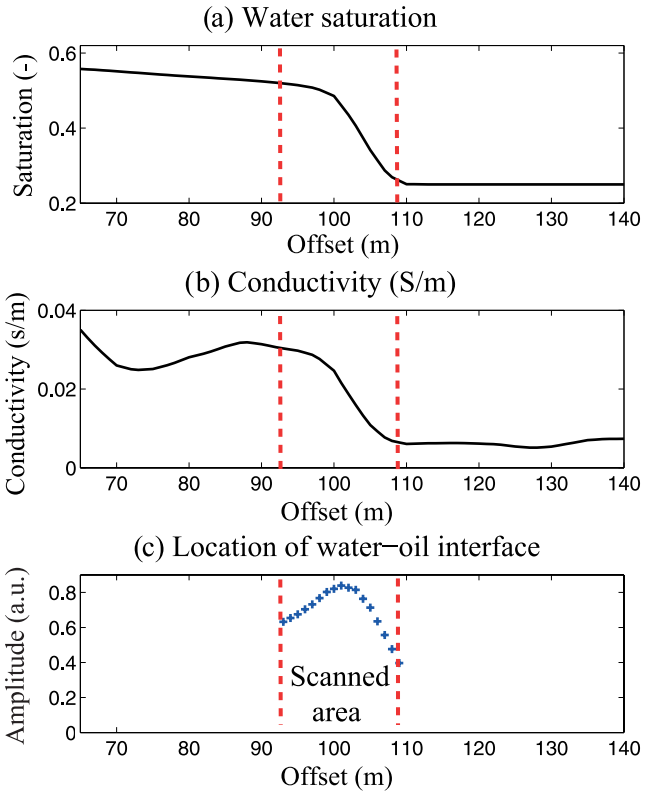


Figure 19. Determination of the position of the oil–water interface using a set of beamforming points at the same depth and crossing the position of the interface. (a) Spatial distribution of the water saturation (snapshot #3) showing the position of the saturation front. (b) Electrical conductivity distribution. (c) Source intensity as a function of offset. This shows that the strongest seismoelectric conversions are generated at the position of the saturation front.

Encouraged by this result, we apply now the seismoelectric beamforming discussed in Section 4 to this case. Figs 18(a)–(e) show the seismic beamforming using the seismic sources located in three wells. Fig. 18(f) shows the resulting electrical potential distribution at the time for which the seismic energy is beamformed. This shows a very strong dipolar field associated with the beamforming.

In Fig. 19, we repeat this operation for a set of scanning pints located at the same depth and crossing the position of the saturation front. Our analysis shows that the strongest seismoelectric conversion is located at the position of the saturation front. Therefore, we can conclude that the scanning of the reservoir could be used to determine the position of the saturation front and to monitor its progression over time. An application of the present theory to a vadose zone case study is also developed in a companion paper (Kulessa *et al*. 2013).

6 CONCLUSIONS

We have developed a simple theory to compute seismoelectric effects in unsaturated conditions. This theory is based on the model of wave propagation in unsaturated media following a straightforward extension of Biot theory that is well accepted. We also developed an even simpler approach based a poroacoustic theory that is also used to compute *P* waves in partially saturated porous media. The electrokinetic part of the model is also consistent with available experimental observations in the laboratory.

The poroacoustic approach is implemented in a finite-element solver with triangular meshing. The capabilities of the forward modelling solver are shown in two cases. The first case is to perform seismic beamforming to localize the presence of heterogeneities in the saturation for a piecewise constant distribution of saturation. The second case corresponds to an enhanced oil-recovery problem. Water is injected in one well and oil is produced in the second well. We show that the seismoelectric method can be used to localize the saturation front using the beamforming approach proposed recently by Sava & Revil (2012). By focusing seismic energy at a given point, we sharply increase the amplitude of the seismoelectric interface response (seismoelectric conversion) with respect to coseismic fields. This is extremely important because, most of the time, the coseismic signals are much stronger, in terms of amplitude, and the seismoelectric conversion barely detectable.

ACKNOWLEDGEMENTS

Funding was provided by the Petroleum Institute of Abu Dhabi. We thank Seth Haines for fruitful discussions and Junwei Zhang for the two-phase flow simulations. Dr. T.K. Young is also thanked for his support at Mines. We thank the Editor Jeannot Trampert, J. Germán Rubino and an anonymous referee for their constructive comments.

REFERENCES

Alkhalifah, T., 1998. Acoustic approximations for processing in transversely isotropic media, *Geophysics,* **63,** 623–631.

Alkhalifah, T., 2000. An acoustic wave equation for anisotropic media, *Geophysics,* **65,** 1239–1250.

Alkhalifah, T., 2003. An acoustic wave equation for orthorhombic anisotropy, *Geophysics,* **68,** 1169–1172.

Araji, A.H., Revil, A., Jardani, A., Minsley, B.J. & Karaoulis, M., 2012. Imaging with cross-hole seismoelectric tomography, *Geophys. J. Int.,* **188,** 1285–1302.

Archie, G.E., 1942. The electrical resistivity log as an aid in determining some reservoir characteristics, *Trans. Am. Inst. Min. Metall. Pet. Eng.,* **146,** 54–62.

Avellaneda, M. & Torquato, S., 1991. Rigorous link between fluid permeability, electrical conductivity, and relaxation times for transport in porous media, *Phys. Fluids A,* **3,** 2529–2540.

Biot, M.A., 1956a. Theory of propagation of elastic waves in a fluid saturated porous solid. I. Low frequency range, *J. acoust. Soc. Am.,* **28,** 168–178.

Biot, M.A., 1956b. Theory of propagation of elastic waves in a fluid saturated porous solid. II. Higher frequency range, *J. acoust. Soc. Am.,* **28,** 179–191.

Brooks, R.H. & Corey, A.T., 1964. *Hydraulic Properties of Porous Media, Hydrology Papers, No. 3,* Colorado State University.

Fourie, F.D., 2003. Application of electroseismic techniques to geohydrological investigations in Karoo Rocks, *PhD thesis*, University of the Free State, Bloemfontein, South Africa, 195 pp.

Garambois, S. & Dietrich, M., 2002. Full waveform numerical simulations of seismoelectromagnetic wave conversions in fluid-saturated stratified porous media, *J. geophys. Res.,* **107**(B7), doi:10.1029/2001JB000316.

Gassmann, F., 1951. Über die elastizität poröser medien: Vierteljahrsschr, *Naturforsch. Ges. Zuerich,* **96,** 1–23.

Guichet, X., Jouniaux, L. & Pozzi, J., 2003. Streaming potential of a sand column in partial saturation conditions, *J. geophys. Res.,* **108,** B32141, doi:10.1029/2001JB001517.

Haartsen, M.W. & Pride, S., 1997. Electroseismic waves from point sources in layered media, *J. geophys. Res.,* **102,** 24 745–24 769.

Haines, S.S., 2004. Seismoelectric imaging of shallow targets, *PhD thesis*, Stanford University, 191 pp.

Hu, H., Guan, W. & Harris, J.M., 2007. Theoretical simulation of electroacoustic borehole logging in a fluid-saturated porous formation, *J. acoust. Soc. Am.,* **122,** 135–145.

Downloaded from http://gji.oxfordjournals.org/ at Colorado School of Mines on July 1, 2015

Huet, C.C., Rushing, J.A., Newsham, K.E. & Blasingame, T.A., 2005. Modified Purcell/Burdine model for estimating absolute permeability from mercury-injection capillary pressure data, in *International Petroleum Technology Conference,* Doha, Qatar, 2005 November 21–23, Paper IPTC 10994, 12 pp.

Hunt, C.W. & Worthington, M.H., 2000. Borehole electrokinetic responses in fracture dominated hydraulically conductive zones, *Geophys. Res. Lett.,* **27,** 1315–1318.

Jardani, A., Revil, A., Slob, E. & Sollner, W., 2010. Stochastic joint inversion of 2D seismic and seismoelectric signals in linear poroelastic materials, *Geophysics,* **75**(1), N19–N31.

Johnson, D.L., Plona, T.J. & Kojima, H., 1986. Probing porous media with 1st sound, 2nd sound, 4th sound and 3rd sound, in *Physics and Chemistry of Porous Media,* Vol. II, pp. 243–277, eds Jayanth, R., Banavar, J. & Winkler, K.W., AIP.

Jougnot, D. & Linde, N., 2013. Self-potentials in partially saturated media: the importance of explicit modeling of electrode effects, *Vadose Zone J.,* **12**(2), doi:10.2136/vzj2012.0169.

Jougnot, D., Revil, A., Lu, N. & Wayllac, A., 2010. Transport properties of the Calloxo-Oxfordian clay-rock under partially saturated conditions, *Water Resour. Res.,* **46,** W08514, doi:10.1029/2009WR008552.

Jougnot, D., Linde, N., Revil, A. & Doussan, C., 2012. Derivation of soil specific streaming potential electrical parameters from hydrodynamic characteristics of partially saturated soils, *Vadoze Zone J.,* **11**(1), doi:10.2136/vzj2011.0086.

Jougnot, D., Rubino, J.G., Rosas Carbajal, M., Linde, N. & Holliger, K., 2013. Seismoelectric effects due to mesoscopic heterogeneities, *Geophys. Res. Lett.,* **40,** doi:10.1002/grl.50472.

Jun-Zhi, W. & Lile, O.B., 1990. Hysteresis of the resistivity index in Berea sandstone, *Advances in Core Evaluation Accuracy and Precision in Reserves Estimation,* Reviewed Proc., in *First Soc. European Core Analysis Symposium,*, London, UK, pp. 427–443, ed. Worthington, P.F., Gordon & Breach Science Publishers.

Karpfinger, F., Müller, T.M. & Gurevich, B., 2009. Green's functions and radiation patterns in poroelastic solids revisited, *Geophys. J. Int.,* **178,** 327–337.

Katz, A.J. & Thompson, A.H., 1987. Prediction of rock electrical conductivity from mercury injection measurements, *J. geophys. Res.,* **92**(B1), 599–607.

Kulessa, B., West, J., McCarthy, P., Revil, A., Mahardika, H., Karaoulis, M. & Jardani, A., 2013. Seismoelectric coupling in unsaturated conditions. 2. Application to the study of the vadose zone, *Geophys. J. Int*.

Leroy, P., Jougnot, D., Revil, A., Lassin, A. & Azaroual, M., 2012. A double-layer model of the gas bubble/water interface, *J. Colloid Interface Sci.,* **388**(1), 243–256.

Li, K. & Horne, R.N., 2005. Inferring relative permeability from resistivity well logging, in *Proceedings of the Thirtieth Workshop on Geothermal Reservoir Engineering Stanford University,* Stanford, California, 2005 January 31–February 2, SGP-TR-176, 6 pp.

Linde, N., Jougnot, D., Revil, A., Matthaı, S.K., Arora, T., Renard, D. & Doussan, C., 2007. Streaming current generation in two-phase flow conditions, *Geophys. Res. Lett.,* **34**(3), L03306, doi:10.1029/2006GL028878.

Maerefat, N.L. & Chang, M.M., 1987. Calibration parameters for resistivty logs, *Preliminary findings, Project BE8, Report for the DOE,* 15 pp.

Mboh, C.M., Huisman, J.A., Zimmermann, E. & Vereecken, H., 2012. Coupled hydrogeophysical inversion of streaming potential signals for unsaturated soil hydraulic properties, *Vadose Zone J.,* **11**(2), doi:10.2136/vzj2011.0115.

Petiau, G., 2000. Second generation of lead-lead chloride electrodes for geophysical applications, *Pure appl. Geophys.,* **3,** 357–382.

Petiau, G. & Dupis, A., 1980. Noise, temperature coefficient and long time stability of electrodes for telluric observations, *Geophys. Prospect.,* **28**(5), 792–804.

Pride, S., 1994. Governing equations for the coupled electromagnetics and acoustics of porous media, *Phys. Rev. B,* **50**(21), 15 678–15 696.

Pride, S.R. & Haartsen, M.W., 1996. Electroseismic wave properties, *J. acoust. Soc. Am.,* **100**(3), 1301–1315.

Purcell, W.R., 1949. Capillary pressures—their measurement using mercury and the calculation of permeability, *Trans. AIME,* **186,** 39.

Revil, A., 2013. Effective conductivity and permittivity of unsaturated porous materials in the frequency range 1 mHz–1GHz, *Water Resour. Res.,* **49,** doi:10.1029/2012WR012700.

Revil, A. & Cathles, L.M., 1999. Permeability of shaly sands, *Water Resour. Res.,* **35**(3), 651–662.

Revil, A. & Cerepi, A., 2004. Streaming potential in two-phase flow condition, *Geophys. Res. Lett.,* **31**(11), L11605, doi:1029/2004GL020140.

Revil, A. & Glover, P.W.J., 1997. Theory of ionic surface electrical conduction in porous media, *Phys. Rev. B.,* **55**(3), 1757–1773.

Revil, A. & Jardani, A., 2010. Seismoelectric response of heavy oil reservoirs. Theory and numerical modelling, *Geophys. J. Int.,* **180,** 781–797.

Revil, A. & Linde, N., 2006. Chemico-electromechanical coupling in microporous media, *J. Coll. Interf. Sci.,* **302,** 682–694.

Revil, A. & Linde, N., 2011. Comment on 'Streaming potential dependence on water-content in Fontainebleau sand' by V. Allegre, L. Jouniaux, F. Lehmann & P. Sailhac, *Geophys. J. Int.,* **186,** 113–114.

Revil, A. & Mahardika, H., 2013. Coupled hydromechanical and electromagnetic disturbances in unsaturated porous materials, *Water Resour. Res.,* **49,** doi:10.1002/wrcr.20092.

Revil, A., Cathles, L.M., Losh, S. & Nunn, J.A., 1998. Electrical conductivity in shaly sands with geophysical applications, *J. geophys. Res.,* **103**(B10), 23 925–23 936.

Revil, A., Linde, N., Cerepi, A., Jougnot, D., Matthäi, S.K. & Finsterle, S., 2007. Electrokinetic coupling in unsaturated porous media, *J. Coll. Interf. Sci.,* **313**(1), 315–327.

Revil, A., Woodruff, W.F. & Lu, N., 2011. Constitutive equations for coupled flows in clay materials, *Water Resour. Res.,* **47,** W05548, doi:10.1029/2010WR010002.

Rubino, J.G. & Holliger, K., 2012. Seismic attenuation and velocity dispersion in heterogeneous partially saturated porous rocks, *Geophys. J. Int.,* **188**(3), doi:10.1111/j.1365–246X.2011.05291.x.

Saunders, J.H., Jackson, M.D. & Pain, C.C., 2008. Fluid flow monitoring in oilfields using downhole measurements of electrokinetic potential, *Geophysics,* **73,** E165–E180.

Sava, P. & Revil, A., 2012. Virtual electrode current injection using seismic focusing and seismoelectric conversion, *Geophys. J. Int.,* **191**(3), 1205–1209.

Talebian, M., Al-Khouri, R. & Sluys, L.J., 2013. Coupled electrokinetic-hydromechanical model for CO_2 sequestration in porous media, *Transp. Porous Media,* **98,** 287–321.

Teja, A.S. & Rice, P., 1981. Generalized corresponding states method for viscosities of liquid mixtures, *Ind. Eng. Chem. Fundam.,* **20,** 77–81.

Thomas, L.K., Katz, D.L. & Tek, M.R., 1968. Threshold pressure phenomena in porous media, *Soc. Petrol. Eng. J.,* **243,** 174–184.

Van Genuchten, M.T., 1980. A closed-form equaton for predicting the hydraulic conductivity of unsaturated soils, *Soil Sci. Soc. Am. J.,* **44,** 892–898.

Vieira, C., Maineult, A. & Zamaro, M., 2012. Laboratory study of self-potential signals during releasing of CO_2 and N_2 plumes, *C. R. Geosci.,* **344**(10), 498–507.

Vinogradov, J. & Jackson, M.D., 2011. Multiphase streaming potential in sandstones saturated with gas/brine and oil/brine during drainage and imbibition, *Geophys. Res. Lett.,* **38,** L01301, doi:10.1029/2010GL045726.

Wang, H.F., 2000. *Theory of Linear Poroelasticity with Applications to Geomechanics and Hydrogeology, Princeton Series in Geophysics,* Princeton University Press, 287 pp.

Warden, S., Garambois, S., Jouniaux, L., Brito, D., Sailhac, P. & Bordes, C., 2013. Seismoelectric wave propagation numerical modelling in partially saturated materials, *Geophys. J. Int.,* **194**(3), 1498–1513.

Waxman, M.H. & Smits, L.J.M., 1968. Electrical conductivities in oil bearing shaly sands, *Soc. Petrol. Eng. J.,* **243,** 107–122.

Wood, A.B., 1930. *A Textbook of Sound,* Macmillan Publishing Co.

Zhu, Z., Toksoz, M.N. & Burns, D.R., 2008. Electroseismic and seismoelectric measurements of rock samples in a water tank, *Geophysics,* **73**(5), E153–E164.

Downloaded from http://gji.oxfordjournals.org/ at Colora Mines on July 1, 2015

APPENDIX: CONDUCTIVITY IN UNSATURATED CONDITIONS

In the absence of an electrical double layer coating the surface of minerals, the conductivity problem is governed at the local scale of the pore space by:

$$\mathbf{j} = -\sigma_w \nabla\psi \text{ in } V_p, \tag{A1}$$

$$\nabla \cdot \mathbf{j} = 0 \text{ on } S, \tag{A2}$$

where $\mathbf{e} = -\nabla\psi$ denotes the local electrical field, ψ the local electrical potential, V_p denotes the pore space and S the solid water interface. In absence of surface conductivity, the boundary-value problem for ψ is therefore given by

$$\nabla^2\psi = 0 \text{ in } V_p, \tag{A3}$$

$$\hat{\mathbf{n}} \cdot \mathbf{e} = 0 \text{ on } S, \tag{A4}$$

$$\psi = \begin{cases} \Delta\Psi & \text{at } z = L \\ 0 & \text{at } z = 0 \end{cases}, \tag{A5}$$

where L denotes the length of the cylindrical representative elementary volume (REV) in the direction of the macroscopic applied electrical field $\mathbf{E} = -(\Delta\Psi/L)\tilde{\mathbf{z}}$, $\Delta\Psi$ denotes the difference of electrical potential between the end-faces of the REV, $\hat{\mathbf{n}}$ is the unit vector normal to the pore water/mineral interface S and V_p denotes the interconnected pore volume. This boundary-value problem can be rewritten in terms of a normalized electrical potential Γ:

$$\nabla^2\Gamma = 0 \text{ in } V_p, \tag{A6}$$

$$\hat{\mathbf{n}} \cdot \nabla\Gamma = 0 \text{ on } S, \tag{A7}$$

$$\Gamma = \begin{cases} L & \text{at } z = L \\ 0 & \text{at } z = 0 \end{cases}, \tag{A8}$$

where the normalized field and potential are written as,

$$\nabla\Gamma \equiv \left(-\frac{\Delta\Psi}{L}\right)^{-1} \mathbf{e}, \tag{A9}$$

and

$$\Gamma \equiv \left(\frac{\Delta\Psi}{L}\right)^{-1} \psi, \tag{A10}$$

respectively. In absence of surface conductivity, the formation factor F is obtained by summing up the Joule dissipation of energy over the pore space,

$$\sigma \left(\frac{\Delta\Psi}{L}\right)^2 = \frac{1}{V}\int_{V_p} \sigma_w |e|^2 \, \mathrm{d}V_p, \tag{A11}$$

which yield the following relationship for the electrical conductivity

$$\sigma = \frac{1}{F}\sigma_w, \tag{A12}$$

$$\frac{1}{F} = \frac{1}{V}\int_{V_p} |\nabla\Gamma|^2 \, \mathrm{d}V_p, \tag{A13}$$

where V is the total volume of the considered REV.

Revil & Glover (1997) extended the use of the Joule dissipation theorem to the case of bulk and surface conduction. The macroscopic Joule dissipation of energy is the sum of all the Joule dissipation contributions occurring at the microscopic scale in both the bulk pore water and in the electrical double layer. This yields,

$$\sigma' \left(\frac{\Delta\Psi}{L}\right)^2 = \frac{1}{V}\int_{V_p} \sigma_w |\mathbf{e}|^2 \, \mathrm{d}V_p + \frac{1}{V}\int_S \Sigma_S |\mathbf{e}|^2 \, \mathrm{d}S, \tag{A14}$$

where Σ_S describes the specific surface conductivity of the electrical diffuse layer (in S) and $\mathbf{e}$ the local electrical field. At high salinity (Dukhin number Du $\ll$1), the distribution of the electrical field is nearly the same as in absence of surface conductivity and, therefore, we have,

$$\sigma = \frac{1}{F}\left(\sigma_w + \frac{2}{\Lambda}\Sigma_S\right), \tag{A15}$$

$$\frac{2}{\Lambda} = \frac{\int_{V_p} |\nabla\Gamma|^2 \, \mathrm{d}V_p}{\int_S |\nabla\Gamma|^2 \, \mathrm{d}S}. \tag{A16}$$

Now the third step is to extend the previous equations to the case where the porous material is partially saturated by water. The second phase, air, is insulating and therefore the air–water interface is characterized by exactly the same boundary conditions than for the water–solid interface. We can define the same boundary-value problem for the normalized potential Γ_w in the pore water phase:

$$\nabla^2\Gamma_w = 0 \text{ in } V_p, \tag{A17}$$

$$\hat{\mathbf{n}} \cdot \nabla\Gamma = 0 \text{ on } S, \tag{A18}$$

$$\Gamma = \begin{cases} L & \text{at } z = L \\ 0 & \text{at } z = 0 \end{cases}, \tag{A19}$$

where S includes now both the air–water and solid–water interfaces. Now the same arguments as above, but taken for the water phase rather than for the complete pore space yield

$$\sigma(s_w) = \frac{1}{F(s_w)}\left(\sigma_w + \frac{2}{\Lambda(s_w)}\Sigma_S\right), \tag{A20}$$

$$\frac{2}{\Lambda(s_w)} = \frac{\int_{V_p} |\nabla\Gamma_w|^2 \, \mathrm{d}V_p}{\int_S |\nabla\Gamma_w|^2 \, \mathrm{d}S}, \tag{A21}$$

$$\frac{1}{F(s_w)} = \frac{1}{V}\int_{V_p} |\nabla\Gamma_w|^2 \, \mathrm{d}V_p. \tag{A22}$$

Like in the case of permeability, the properties $\Lambda(s_w)$ and $F(s_w)$ are expected to be breakable into the product of a value at saturation and a function of the saturation itself.

Downloaded from http://gji.oxfordjournals.org/ at Colorado School of Mines on July 1, 2015